water

MDPI

Article

Estimation of ET and Crop Water Productivity in a Semi-Arid Region Using a Large Aperture Scintillometer and Remote Sensing-Based SETMI Model

Pragya Singh [1,*], Vinay Kumar Sehgal [1], Rajkumar Dhakar [1], Christopher M. U. Neale [2], Ivo Zution Goncalves [2], Alka Rani [1], Prakash Kumar Jha [3], Deb Kumar Das [1], Joydeep Mukherjee [1], Manoj Khanna [4] and Swatantra Kumar Dubey [5]

1 Division of Agricultural Physics, ICAR-Indian Agricultural Research Institute, New Delhi 110012, India; vksehgal@gmail.com (V.K.S.); rajdhakar.iari@gmail.com (R.D.); alka411192@gmail.com (A.R.); dkdas.iari@gmail.com (D.K.D.); joydeep.icar@gmail.com (J.M.)
2 Daugherty Water for Food Global Institute, University of Nebraska, Lincoln, NE 68508, USA; cneale2@unl.edu (C.M.U.N.); ivo.zution@gmail.com (I.Z.G.)
3 Department of Plant and Soil Sciences, Mississippi State University, Starkville, MS 39762, USA; pj442@msstate.edu
4 Water Technology Centre, ICAR-Indian Agricultural Research Institute, New Delhi 110012, India; khanna_manoj2001@yahoo.com
5 Department of Environmental Engineering, Seoul National University of Science and Technology, Seoul 01811, Republic of Korea; swatantratech1@gmail.com
* Correspondence: prgsingh10@gmail.com

Abstract: With the increasing water scarcity and the demand for sustainable agriculture, precise estimation of crop evapotranspiration (ET) is crucial for effective irrigation management, crop yield assessment, and equitable water distribution, particularly in semi-arid regions. In this study, a large aperture scintillometer (LAS) was used to validate the remote sensing-based ET model SETMI (Spatial Evapotranspiration Modeling Interface) in an irrigated maize-wheat cropping system in a semi-arid region at the ICAR-Indian Agricultural Research Institute, New Delhi. Results obtained by the SETMI model depicted modeled surface energy fluxes compared well with LAS field data, showing a very high R^2 (0.83–0.95) and NRMSE (8–29%). The SETMI model performed better in the case of the maize crop than the wheat crop in field experiments. Further, the SETMI model was employed at the regional level using high-resolution Sentinel-2 to estimate the regional water productivity of wheat crops over a semi-arid region in India. The estimated regional, seasonal wheat actual ET mainly ranged between 101 mm and 325 mm. The regional wheat water productivity varied from 0.9 kg m^{-3} to 2.20 kg m^{-3}. Our research reveals that the SETMI model can give reliable estimates of regional wheat water productivity by examining its spatial and temporal fluctuations and facilitating the creation of regional benchmark values.

Keywords: evapotranspiration; large aperture scintillometer; maize; SETMI; semi-arid; water productivity; wheat

check for updates

Citation: Singh, P.; Sehgal, V.K.; Dhakar, R.; Neale, C.M.U.; Goncalves, I.Z.; Rani, A.; Jha, P.K.; Das, D.K.; Mukherjee, J.; Khanna, M.; et al. Estimation of ET and Crop Water Productivity in a Semi-Arid Region Using a Large Aperture Scintillometer and Remote Sensing-Based SETMI Model. *Water* **2024**, *16*, 422. https://doi.org/10.3390/w16030422

Academic Editor: Guido D'Urso

Received: 4 January 2024
Revised: 22 January 2024
Accepted: 24 January 2024
Published: 28 January 2024

1. Introduction

The arid and semi-arid regions occupy approximately one-third of the planet's surface, where water supplies are generally limited, and it is challenging to meet industrial, agricultural, and ecological water demands. Most of these regions face water resource pressures driven by water consumption from irrigated agriculture [1]. Climate change exacerbates water scarcity issues in semi-arid areas [2]. Hence, there is an immediate requirement to manage water resources for sustainable crop production. Estimating crop evapotranspiration is one of the ways to manage water resources due to its essential role in irrigation scheduling and crop water productivity estimation. Field-scale ET measurement systems

include lysimeters, Bowen ratios, eddy covariance systems, surface renewal systems, and classical soil water balancing [3,4]. Though these methods are more accurate, they are costly, provide field-specific measurements only, and must be extrapolated or interpolated with limited accuracy [5]. Large aperture scintillometry (LAS) is a recent field measurement technique to estimate crop evapotranspiration (ET) by estimating areal-averaged sensible heat fluxes over spatial distances nearly equivalent to those observed by satellites [6,7]. LAS-based ET measurements can validate satellite-based ET estimates over larger regions. The estimate of ET using remote sensing technologies has also received growing interest in research [8,9].

Thus, remote sensing images are progressively being employed to assess evapotranspiration (ET) across various spatial and temporal extents. Over the past twenty years, numerous models have been developed to estimate evapotranspiration using remotely acquired data [10–12]. A few of these models include SEBAL (Surface Energy Balance Algorithm for Land) [13,14], SEBS (Surface Energy Balance System) [15], METRIC (Mapping EvapoTranspiration at high Resolution with Internalized Calibration) [16], and SSEBop (Operational Simplified Surface Energy Balance) models [17,18]. These models can be categorized into one-source models and two-source models. One-source surface energy balance-based ET models simulate bulk ET from the land surface primarily using remotely sensed land surface temperature (LST) and vegetation index (VI) [14,15,19]. However, the two-source model describes physical processes and simulates spatial explicit evaporation (E) and transpiration (T) individually [19,20], which proves to be better for comprehending agricultural processes. SETMI (Spatially ET Mapping Interface) is a recent hybrid ET model that is a combination of the model of Norman et al. [19] two-source energy balance (TSEB) ET model with a water balance (WB) model using reflectance-based crop coefficients (K_{cbrf}).

Crop ET is important to assess disparity in agricultural production among various regions in terms of both land productivity and water productivity [21]. Crop water productivity is an important step toward connecting water management to larger stated goals such as water security, food security, and economic growth. Although boosting crop water productivity can help solve the water and food crises, it is more challenging to accomplish crop water productivity gains at the farm level, partly because standard values are lacking, and farmers are not led by any methods [22]. Much information is linked with agricultural productivity, but more information and recommendations on WP (kg m^{-3}) must be provided. Traditional approaches rarely give reliable estimates of spatial ET, often confined to small regions and mainly focusing on vulnerable and vital areas. This indicates the significance of regional-scale research, which would aid in many key water management and agricultural policy decisions at this level. Notably, water is likely to be a more constraining limitation for Indian agriculture [23]. So, it is time to shift the paradigm from increasing agricultural production per unit of land to improving agricultural productivity per water unit. Estimates of yield (Y) and ET based on remote sensing enable us to construct populations of WP data from which yield and water productivity gaps may be computed [24].

The objective of this study includes using the SETMI model for estimating crop evapotranspiration (ET) for a maize-wheat cropping system in a semi-arid irrigated area and its validation with LAS estimates, estimating regional wheat crop yield in selected three semi-arid zones and their regional wheat water productivity in the northwestern region of India. This study reveals high-performing and low-performing WP clusters in India's northwest area. Furthermore, individuals and organizations may utilize the data to designate strategic areas, establish development objectives, and rationalize funding or policies to increase crop water productivity.

2. Materials and Methods

2.1. Study Area

A field experiment was carried out in the ICAR-Indian Agricultural Research Institute Farm, New Delhi (28°38′23″ N and 77°09′27″ E), for two years (2015–2016 over cropping

seasons in rainy (*kharif*) and winter (*rabi*); winter season 2016–2017 and the rainy season 2017–2018 (Figure 1). Maize (corn) was selected as the *kharif* season crop, and wheat as the *rabi* crop for the field experiment to estimate crop ET. The region's climate is semi-arid and subtropical, with chilly winters and hot-dry summers, and the area has sandy loam soil. The average annual rainfall in the New Delhi area is 769.3 mm, with more than 75 percent received between June and September (southwest monsoon) and only 63.5 mm received during winter (western disturbances).

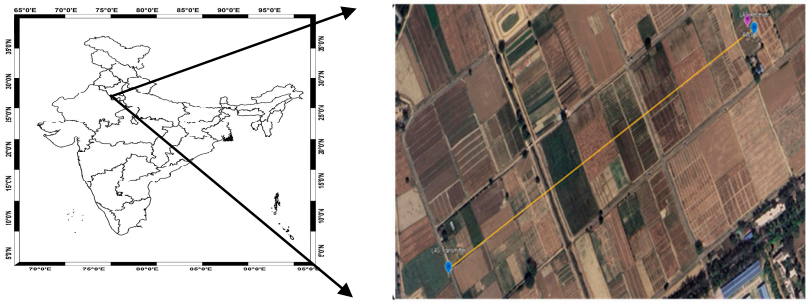

Figure 1. The study area is in New Delhi, India, and the LAS path footprint is overlaid on the satellite image of the ICAR-IARI research farm.

Furthermore, to calculate wheat crop water productivity, three regions in the north-western parts of India were selected (Jhajjar, Gurugram, and Rohtak districts of Haryana state) (Figure 2). According to the Koppen classification, the climate of the Jhajjar district is tropical steppe, semi-arid, and hot, with extreme air dryness except during monsoon months, intensely hot summers, and cold winters [25]. Similarly, Rohtak district falls under the sub-humid and semi-arid/arid zones, and it experiences extremely hot and dry summers and chilly winters [26]. Moreover, Gurugram district's climate is tropical steppe, semi-arid, and hot, and it is primarily distinguished by arid air (except during the monsoon season), extremely hot summers, and cold winters [27]. The southwest monsoon provides the most rainfall (>75%) from July to September. However, western disturbances also contribute a small amount of precipitation during the winter season in these three regions. These regions primarily receive annual rainfall between 550 and 700 mm. The soils of the study region range in texture from coarse loamy to fine loamy. These districts were selected because they use various irrigation techniques, including rainfed, groundwater, and canal irrigation. Due to the region's low and irregular rainfall, water scarcity in canals, high evaporative demands, sandy soils with little water holding capacity, medium to poor groundwater quality, and fluctuating groundwater levels, water management in the study area is complicated.

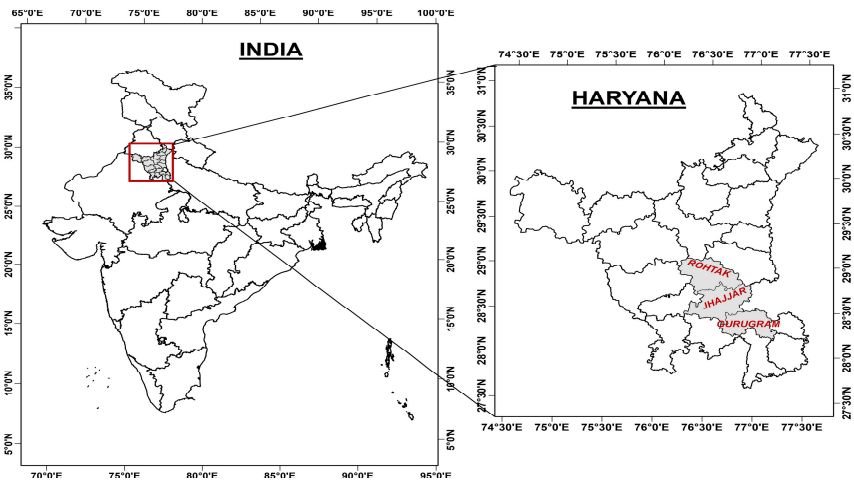

Figure 2. Map showing the three study districts in Haryana: Rohtak, Jhajjar, and Gurugram.

2.2. Micrometeorology Sensors and Measurements

An automatic weather station (AWS) at the agrometeorology observatory (Class-A) having sensors of net radiometer, anemometer (two levels), temperature and humidity probes (two heights), and soil heat flux plate at 10 cm depth was added along the LAS path length in IARI, New Delhi farm. AWS measured daily weather information such as ground heat flux (G), net radiation (Rn), minimum and maximum temperature, wind speed and direction, relative humidity, global radiation, etc. Meteorological parameters were recorded by sensors (Table 1) in AWS regularly at 5-min intervals in synchronization with LAS sensible heat fluxes (H) measurements. As Rn and G were recorded at 5-min intervals using a net radiometer and ground heat flux plate, respectively, the 5-min fluxes of LE (Wm^{-2}) were calculated by merging LAS with AWS measurements in the EVATION software (V2R5).

Table 1. Sensors were used during the field experiment for 2015–2016, 2016 (*rabi*), and 2017 (*Kharif*).

S. No.	Observation/Measurement	Parameter Measured	Sensor Used	Model Type
1.	Surface energy flux	Sensible heat flux (H)	Large-aperture scintillometer	Kipp & Zonen: MKII, Delft, Netherland
2.	Radiation	Net radiation (Rn) Incoming global radiation	Net radiometer Pyranometer	Kipp & Zonen: NR-LITE/CNR4, Delft, Netherland Kipp & Zonen:CMP3, Delft, Netherland
3.	Two levels of meteorological parameters (2 m and 4 m above ground)	Wind speed and direction Relative Humidity Air temperature	Anemometer and wind vane Humidity probe Temperature probe	R M Young: 05103-L Campbell Scientific: CS 215, UT, Logan, UT, USA Campbell Scientific: CS 215, Logan, UT, USA
4.	Biophysical measurements	Leaf Area Index	Plant canopy analyzer	LI-COR: LAI 2000, Lincoln, NE
5.	Soil measurements	Soil moisture Ground Heat Flux (10 cm depth)	Time domain reflectometer Soil Heat Flux Plate	Spectrum Tech: Fieldscout 300, Aurora, IL, USA Hukseflux: HFP015C, Delft, Netherland
6.	Data recording	Data logging and storage	Datalogger	Campbell Scientific: CR-1000, Logan, UT, USA

2.3. Energy Fluxes: Observation/Estimation

A large aperture scintillometer (LAS) (Make: Kipp & Zonen LAS MkII) was installed at the ICAR-IARI research farm in December 2013 at 4.5 m above ground in the northeast and southwest directions, covering a path length of 990 m. It has a transmitter and receiver, with a 10 cm aperture, and a built-in data recorder in the receiver, monitoring the sensible heat flux (H) every five minutes throughout the path length. Continuous measurements of energy fluxes from combining LAS and AWS were analyzed at 5-min intervals and averaged hourly to depict the daily behavior of Rn, H, LE, and G. The estimation of surface energy flux was dominated by the central portion of the LAS path length.

2.4. Field Observation and Measurements

During the crop growing season, field measurements (along the 990 m path length of the LAS) of soil moisture, leaf area index (LAI), plant height, and crop phenological stages were taken fortnightly. Field Scout TDR 350 (Spectrum Technologies, Aurora, IL, USA) has been used to measure the top 12 cm of soil surface moisture on a volume basis. The plant canopy analyzer (LAI-2000) instrument LICOR (Lincoln, NE, USA) was used to estimate the crop LAI non-destructively in the field. After removing outliers, the average crop field LAI for a given day was calculated by averaging several LAI readings from that field. The phenological stages of the crops (maize (*Kharif*) and wheat (*rabi*)) were observed, and their dates were noted. On the observation day, six plants at random from a plot were selected to measure the height of the plants using a metric scale, and the average plant height for that plot was calculated from the six values for both maize and wheat crops. Over 70 readings along the LAS path length were taken in two experimental years (crop

and soil) to obtain a site-representative value for the biophysical parameters. A weighted average was computed to obtain a single figure based on the area a crop type occupies.

2.5. Spatial Evapotranspiration Modeling Interface (SETMI) Model

The Spatial Evapotranspiration Modeling Interface (SETMI) [28,29] is a hybrid model that combines the Two-Source Energy Balance (TSEB) model [19] and the soil water balance (WB) model (which employs spectral reflectance-dependent crop coefficients). The SETMI is embedded in ESRI's (Redlands, CA, USA) geographic information system (GIS) software, ArcGIS 10.4. It has three main phases: (1) preparation of a database; (2) model calculation and data analysis; and (3) system tools and outputs. Each stage comprises several steps supported by the tools and functions of ArcGIS (10.4.1) and ERDAS IMAGINE software 2014. The complete methodology to estimate crop ET by the SETMI model is illustrated in Figure 3.

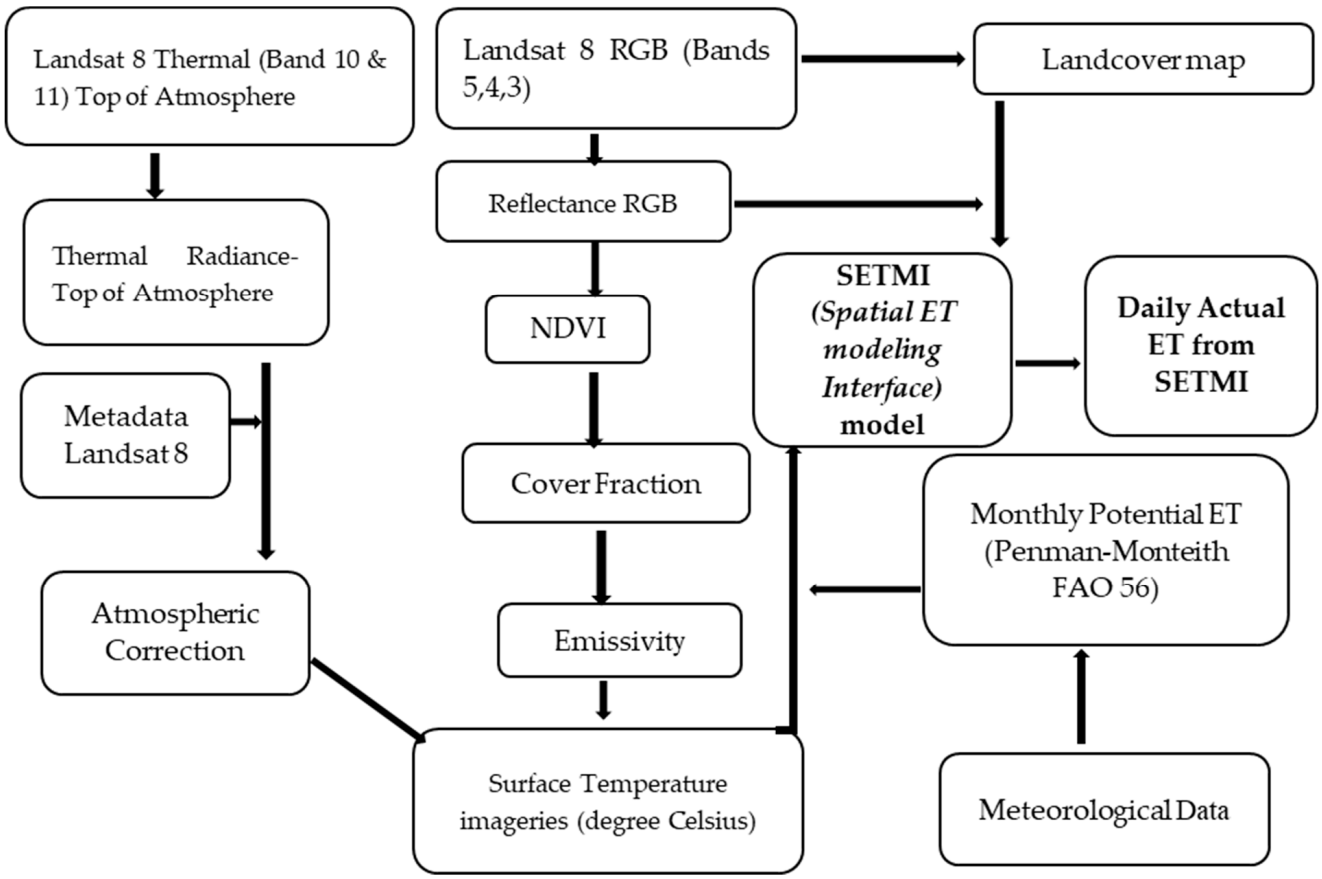

Figure 3. Flowchart of the methodology used in the ET estimation using the SETMI model.

The two-source energy balance model estimates the fluxes by partitioning the total energy received at the Earth's surface into its respective components of net radiation and sensible, latent, and soil heat flux using surface energy balance. It computes soil and vegetation's surface energy balance components separately, requiring the input of radiometric surface temperature observations in the model. However, TSEB necessitates thermal infrared imagery, which limits its application to image collection dates (e.g., satellite overpass). Our study used only the TSEB model embedded in SETMI to derive the actual crop ET since the soil water balance model could not be calibrated effectively. The model parameters were calibrated locally, which are mentioned in Table 2.

Table 2. Values of parameters used in the SETMI Model for maize and wheat crops.

S. No.	Parameters	Values
1.	*αleaf* VIS (leaf absorptivity in the visible range)	0.49–0.85
2.	*αleaf NI* (leaf absorptivity in the NIR range)	0.15–0.30
3.	*αleaf TI* (leaf absorptivity in the TIR range)	0.60–0.95
4.	*αleaf Dead* VIS (absorptivity of dead leaves in the visible range)	0.30–0.49
5.	*αleaf Dead* NIR (absorptivity of dead leaves in the near-infrared range)	0.10–0.13
6.	*αleaf Dead* TIR (absorptivity of dead leaves in the thermal infrared range)	0.80–0.95
7.	Fg (fraction of green leaves)	0.15–0.60
8.	Hc min (minimum canopy height) (m)	0.1
9.	Hc max (maximum canopy height) (m)	1.2–2.5
10.	S (leaf size width) (m)	0.05–0.20
11.	Wc (canopy width) (m)	0.22–0.90
12.	LAI (leaf area index)	0.1–4.5
13.	Refl soil VIS (soil reflectivity in the visible range)	0.25
14.	Refl soil NIR (soil reflectivity in the NIR range)	0.15–0.25
15.	ε soil TIR (soil emissivity in the TIR range)	0.95–0.99
16.	Ag (ratio of soil heat flux to canopy net radiation)	0.3–0.4
17.	D (ratio of crop height and canopy width)	1–3

Note: α—absorptivity of green leaves in the visible range, used in the net radiation model of Campbell and Norman, S—used within the TSEB to calculate the extinction coefficient.

The difference between soil/plant and atmospheric conditions is accounted for by TSEB (two-source energy balance). Additionally, it also accommodates off-nadir thermal sensor view angles. In addition to providing details on stress and soil/plant fluxes, the difference between net radiation and the sum of the sensible and ground heat fluxes yields the latent heat flux, which is presented as equations below:

$$T_{RAD}\ (\theta) \backsim fc(\theta) \times Tc + 1 - fc(\theta) \times Ts$$

$$LE = Rn - (H + G)$$

where T_{RAD} is the radiative temperature recorded by the thermal sensor at view angle θ, Tc is canopy temperature, Ts is soil temperature, and fc is canopy fraction covering the ground, which acts as a weighting function between Tc and Ts. Table 3 lists the vegetation absorptivity utilized in the net radiation (Rn) model calculations.

Table 3. Net radiation parameters used in the TSEB model (SETMI) for maize and wheat crops [30].

Surface Type	Absorptivity		Emissivity
	Visible	Near Infrared	
Green vegetation	0.85	0.20	0.98
Senesced vegetation	0.49	0.13	0.95
Soil	0.15	0.25	0.93

Instantaneous latent heat flux (LE) computed using the TSEB is then scaled to a daily actual ET value following Chavez et al. [31] using the instantaneous and daily reference ET ratio according to the equation:

$$ETd = LEi \times \left(\frac{3600}{\lambda}\right) \times \left(\frac{ETo,d}{ETo,i}\right)$$

where ETd represents daily actual evapotranspiration (mm/day); ETr represents reference evapotranspiration (mm); LE represents latent heat flux (W m^{-2}); λ denotes latent heat of evaporation (W m^{-2}) [30]. The subscripts d and i stand for daily and instantaneous values, respectively. A more detailed description of the SETMI model can be found in the work of [31,32].

2.6. Validation of the SETMI Model with a Large Aperture Scintillometer (LAS)

2.6.1. Model Input Parameters

(a) Remote sensing imagery

The remote sensing imageries were obtained from the Landsat 8 operational land imager (OLI) and Landsat 8 thermal infrared sensor (https://earthexplorer.usgs.gov/ (accessed on 3 January 2024)). The ortho-rectified Level 1T images of Landsat 8 were pre-processed for atmospheric and radiometric corrections. The Level 1T product's coefficients were used to undertake radiometric calibration. Web applications [33] were used to perform atmospheric corrections of thermal infrared imagery using surface emissivity values. Local ground data from the site's weather station and atmospheric profiles that were interpolated to the location were employed for this purpose. Computing the vegetation cover fraction is required for atmospheric corrections [34]. Based on previous local Landsat 8 images, we utilized a minimum NDVI of 0.2 and a maximum value of 0.9 to compute this. ERDAS IMAGINE 2014 and ArcGIS 10.4.1 software were used to pre-process the images.

A list of the cloud-free Landsat 8 images used as input in the SETMI model is provided in Table 4. A challenge in this study was the infrequency of cloud-free satellite images due to clouds, especially in the rainy season, and fog in the winter. The ICAR-IARI experimental field was in a Landsat 8 image overlap zone. Even though this doubled the frequency of satellite overpasses, the non-availability of cloud-free images reduced the overall frequency of pictures used. The SETMI interface was used to input land cover information, which is needed for the computation of ET for each satellite pass date by the TSEB. This input consists of surface temperature (Landsat 8 band 10), meteorological data for the research area, and Landsat 8 bands 3, 4, and 5 (converted to reflectance and atmospherically corrected).

Table 4. List of cloud-free Landsat 8 images used in the SETMI model.

S. No.	2015–2016 (Rainy/*kharif*)	2015–2016 (Winter/*rabi*)	2017–2018 (Rainy/*kharif*)	2016–2017 (Winter/*rabi*)
1.	30 August 2015	11 November 2015	25 June 2017	15 December 2016
2.	8 September 2015	4 December 2015	4 September 2017	22 December 2016
3.	24 September 2015	30 January 2016	13 September 2017	24 February 2017
4.	1 October 2015	2 March 2016	20 September 2017	5 March 2017
5.	10 October 2015	9 March 2016	29 September 2017	12 March 2017
6.	17 October 2015		6 October 2017	21 March 2017
7.	26 October 2015		15 October 2017	28 March 2017
8.			22 October 2017	6 April 2017

(b) Ground input parameters

The air temperature, incident solar radiation, wind speed, and vapor pressure were computed in real time by the SETMI model. Scaling estimated instantaneous LE to daily ET values required the addition of immediate and daily total ETr [31]. For this reason, we used point weather data. Using the ASCE Standardized Reference ET equation for a tall reference crop [35] and REF-ET software (version 4.1.4.22.2016), the ETr was computed at an hourly time step. Thus, using ground weather data, we calculated reference evapotranspiration (ETr) for the day of the satellite's passage, which was then multiplied by the mean Kc (crop coefficients) in the study area using the Reference Evapotranspiration Calculator (RefET [35]). The SETMI calculations were performed on a 1-m scale for both the maize and wheat crops. The plot values of the SETMI ET were calculated by averaging the small pixels within each plot; as the vegetation-index-based peak predicted crop height started to decline, a crop height at the peak value was kept for a specific pixel. Despite the intention to retain the peak value, the leaf area index still needed to be maintained at its highest level in September. To improve consistency between years, the peak leaf area index for the season for a given pixel was utilized in post-processing after August in the case of the maize crop.

(c) Weather input parameters

The autonomous weather station established at Agromet Observatory ICAR-IARI provided the 5-min interval, hourly, and daily readings that the SETMI model required.

2.6.2. Evaluation of Model-Estimated Parameters

The model validation primarily compared modeled ET and surface energy fluxes with measured ET and energy fluxes from a large aperture scintillometer (LAS) at our ICAR-IARI, New Delhi, research field. The estimated spatial surface energy fluxes from the SETMI were combined and compared to ground-based LAS-observed fluxes. The predicted and measured instantaneous LE (W m^{-2}) were compared after being extrapolated to equal daily ET (mm day^{-1}). The reference ET fraction (ETrF) approach, which was introduced and used by Chavez et al. [31], was used to extrapolate the instantaneous ET. ETrF, which is assumed to remain constant throughout the day, is the ratio between the instantaneous values of SETMI ET or LAS ET and ground-based measured ETr. To extrapolate to the daily SETMI ET, the relevant ETrF is multiplied by the daily ETr. Additionally, LAS estimated H (W m^{-2}), net radiation obtained from a pyranometer, and soil heat flux received from soil heat plates attached to the automatic weather station were used to validate the SETMI estimated sensible heat flux H (W m^{-2}), net radiation, and ground heat flux (W m^{-2}). The root mean square error (RMSE), coefficient of determination (R^2), mean bias error (MBE), and normalized root mean square error (NRMSE) were used to evaluate the model performance statistics. An R^2 value close to unity shows that model estimation has a low error variance. A lower NRMSE value closer to zero is desirable to imply that the model can predict with lower error and vice versa [32]. Similarly, a low MBE value indicates a lower model prediction error, while a negative MBE indicates that the model is underestimated, while a positive mean is overestimated.

2.7. Estimation of Regional and Seasonal ET of the Wheat Crop for the Winter Season (Rabi) 2018–2019

When daily ET is unavailable due to the temporal resolution of satellites and gaps in image acquisition due to cloud cover over the area of interest, the computation of seasonal/annual ET based on remote sensing is complicated. Numerous methods exist to extrapolate instantaneous ET to daily ET [31], but there are limited options for extrapolating daily ET to seasonal or annual ET. One way of estimating seasonal ET is to use the linear method to compute monthly and seasonal ET based on the calculated daily ET on the days of satellite acquisition. Therefore, we estimated seasonal ET over the three study area districts using the methodology described below. Landsat 8 OLI images were acquired and atmospherically corrected for the research area using a technique similar to that explained earlier. The weather stations in the research area provided the ground weather data. Reference ET estimation was calculated using REF-ET software, as explained earlier. These parameters were used as input in the validated SETMI model, which was then run over all three districts of the studied area to obtain daily ET (mm/day).

2.7.1. Estimation of ETrF between Days of Satellite Image Acquisitions

We used the accumulated alfalfa-referenced ET (ETr) and the ETrF for the image date to calculate the seasonal actual ET. Hourly and daily ETr were computed with the help of hourly meteorological data obtained from the automatic weather station installed in the study region. The REF-ET software was used to calculate hourly ETr using the hourly meteorological data, which was further summed over 24 h to obtain the daily ETr values. Thus, the reference ET fraction (ETrF) was calculated based on ETins and alfalfa-referenced ET (ETr, mm h^{-1}) from the weather data as follows:

$$ETrF = ET_{ins}/ETr$$

Finally, the daily ET (ET24, mm day^{-1}) at each pixel within the image was calculated using the equation:

$$ET_{24} = ETrF \times ETr_{24}$$

ETr24 is the alfalfa-referenced daily ET (mm day^{-1}) based on summed-up hourly ETr.

2.7.2. Estimation of Monthly and Seasonal Evapotranspiration

ETa is best computed daily and added to the total crop-growing periods. Due to the absence of daily high-resolution images, this is not feasible. Thus, our research employed a linear method to compute monthly ET using model-estimated daily ET values. The representative ETrF was multiplied by the corresponding Etr value to compute the daily ET for a particular day. The monthly ET was calculated by adding the daily computed ET values, and the seasonal value was computed by summing the monthly ET (Figure 4). Thus, linear EtrF interpolations between the acquisition dates of the processed images were performed to estimate the seasonal ET. These values were then multiplied by the daily ETr. Thus, monthly and seasonal ET were calculated by linearly interpolating the ETrF values for the intervals between two consecutive images. It is crucial to obtain a reasonable estimation of the daily ET because it is utilized to compute the seasonal ET on the days of the satellite overpass. Also, it is necessary to consider that errors caused by overestimating and underestimating daily ET are rectified while computing seasonal ET. In the linear interpolation, the slope of the line at the image dates is discontinuous. The previously outlined method is applicable if satellite images are regularly available and model estimates can identify the ET variation pattern.

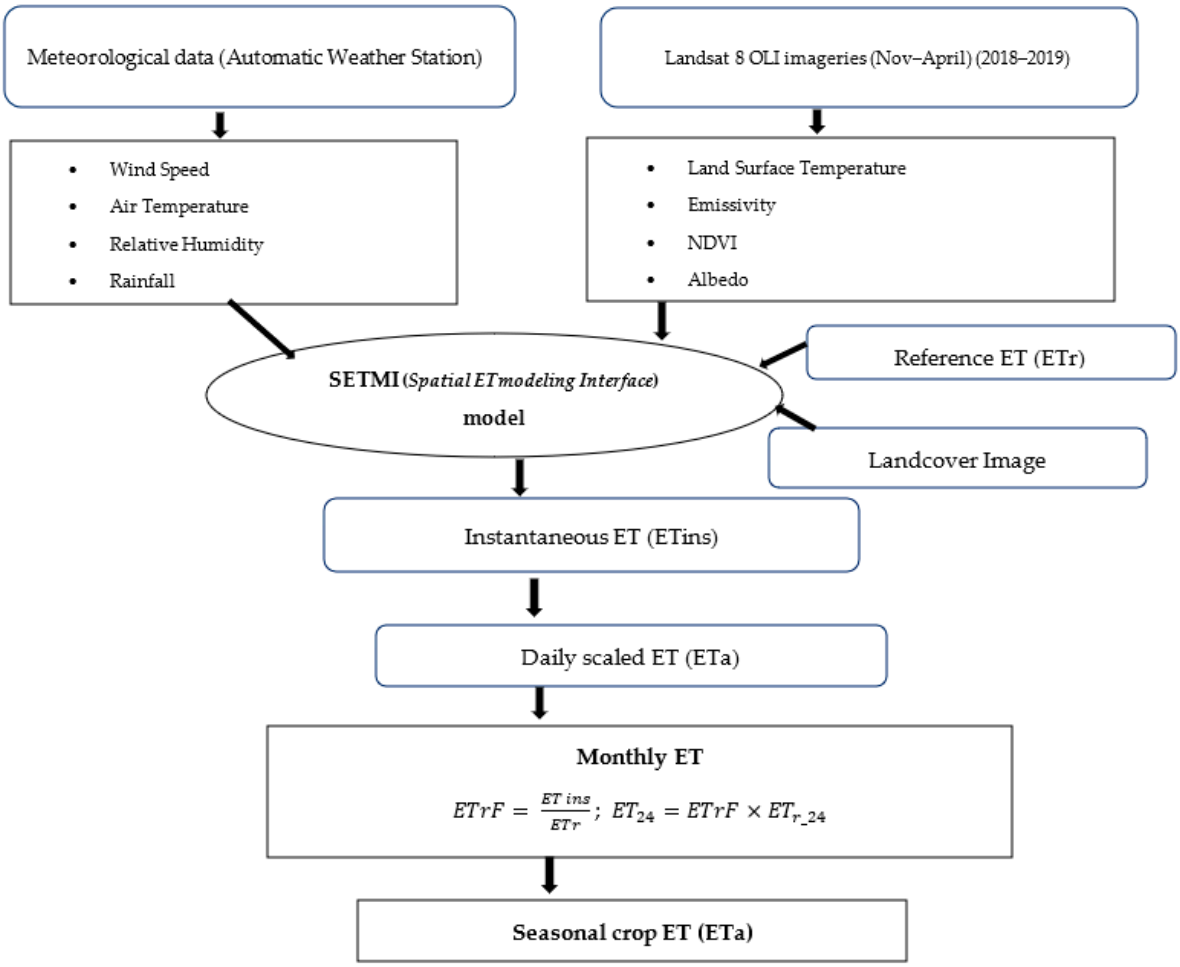

Figure 4. The proposed scheme for remote sensing-based estimation of regional ETa (seasonal actual evapotranspiration) for wheat crops in a semi-arid region.

2.8. Estimation of Regional Wheat Yield for the Winter Season (Rabi) 2018–2019

Estimation of Net Primary Productivity (NPP) of Wheat Crop

From the perspective of carbon trapping and allocation to yield qualities, photosynthesis relates to insolation and productivity. Net primary productivity (NPP) is the most significant of the various measures of primary production in terms of carbon. For this experiment, to estimate the NPP of wheat during the winter/*rabi* season of 2018–2019, a top-down method was used to simulate the NPP of three districts (Rohtak, Jhajjar, and Gurugram). The procedure used environmental downregulations caused by soil moisture and air temperature coupled with a production efficiency modeling (PEM) methodology. The entire process of estimating the predicted yield is well depicted in Figure 5.

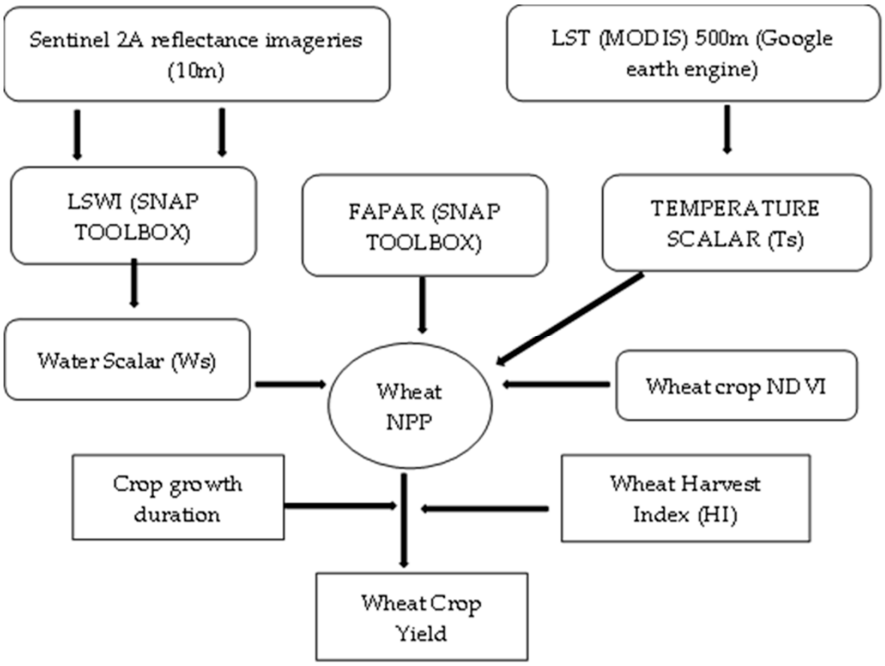

Figure 5. Methodology for wheat NPP and yield estimation using RS based on the production efficiency method approach (PEM) approach.

(a) NPP model (Production Efficiency Modeling Approach)

In the LUE (light use efficiency) approach [36], NPP is the product of absorbed photosynthetically active radiation (APAR) absorbed by the vegetation canopy and light use efficiency (LUE):

$$\text{NPP} = \text{APAR} \times \text{LUE}$$

where NPP is the net primary productivity (g dry mass (DM) m^{-2} $time^{-1}$), APAR stands for absorbed photosynthetically active radiation (MJ m^{-2} $time^{-1}$), and LUE is light use efficiency (g MJ^{-1}). Here, the APAR used is a product of incident PAR and a fraction of absorbed PAR (FAPAR), which is quantifiable from remote sensing. FAPAR generally has a strong linear relationship with the NDVI.

(b) Down-regulation of maximum LUE

LUE varies spatially across different vegetation types and temporally within the individual plant or biome types due to variable temperature and moisture conditions. An assumption made for constant LUE in NPP estimation needs to be revised. Therefore, maximum LUE is downregulated during times of moisture and temperature stress. The LUE, thus, was calculated with the help of the following equation [37]:

$$\text{LUE} = \varepsilon^* \text{Ts}^* \text{Ws}$$

where ε* stands for the maximum light use efficiency of the wheat crop taken as 2.8 g/MJ, and Ts and Ws stand for temperature and water stress scalars, respectively.

(c) Satellite data pre-processing

This study employed data from the Sentinel-2 multi-spectral imager (MSI) with 20 m spatial resolution and the Landsat 8 operational land imager (OLI) with 30 m spatial resolution for the three districts (Table 5). For these three districts, Sentinal-2A MSI and Landsat 8 OLI satellite data were obtained during the wheat crop's growth season (2018–2019) (Tables 6 and 7, respectively). The images were utilized to run a SNAP toolbox to estimate the biophysical parameters of the selected districts. With only a 10-min transit time difference, the Landsat 8 OLI and Sentinel-2 MSI images used in this investigation had illumination and solar zenith angles quite close. Additionally, both sensors have similar viewing angles close to the nadir and have the exact same radiometric resolution (12 bits). Sentinel-2A images for the three districts were downloaded from the Copernicus website (https://scihub.copernicus.eu/ (accessed on 24 December 2019)). All ten bands at 30 m resolution were created by resampling the four bands at 10 m to 30 m spatial resolution. In the current study, nine spectral bands (blue (B2), green (B3), red (B4), red edge 1 (B5), red edge 2 (B6), VNIR (B7), NIR (B8a), SWIR 1 (B11), and SWIR 2 (B12)) were used in combinations for FPAR and LSWI retrieval.

Table 5. Operational satellites with medium to high spatial resolution used for the NPP estimation for the wheat crop (2018–2019).

S. No.	Satellite	Sensor	Time Resolution	Image Size	Product	Spatial Resolution
1.	Landstat-8	OLI (operational land imager) TIRS (thermal infrared sensor)	16 days	185 km × 180 km	L1TP	30 m and 100 m
2.	Sentinel-2A	MSI (multispectral instrument)	15 days	290 km × 290 km	L1C	20 m (resampled at 30 m)

Table 6. Sentinel-2A images date for Rohtak, Jhajjar, and Gurugram during the winter (*Rabi*) season (2018–2019).

S. No.	Rohtak and Jhajjar	Gurugram
1.	26 November 2018	26 November 2018
2.	29 January 2019	5 December 2018
3.	18 March 2019	21 December 2018
4.	3 April 2019	29 January 2019
5.	19 April 2019	23 February 2019
6.		11 March 2019
7.		18 March 2019
8.		3 April 2019

Table 7. Landsat 8 OLI images were used for estimating wheat ET and WP for three districts of Haryana (Rohtak, Jhajjar, and Gurugram).

S. No.	Rohtak and Jhajjar	Gurugram
1.	23 November 2018	16 November 2018
2.	9 December 2018	23 November 2018
3.	25 December 2018	2 December 2018
4.	10 January 2019	9 December 2018
5.	27 February 2019	18 December 2018
6.	31 March 2019	25 December 2018
7.		10 January 2019
8.		19 January 2019
9.		4 February 2019
10.		20 February 2019
11.		27 February 2019
12.		8 March 2019
13.		24 March 2019
14.		31 March 2019
15.		25 April 2019

The biophysical processor of the Sentinel-2 Toolbox software (5.6.0) computes Level-2B biophysical products like LAI FAPAR using atmospherically corrected MSI images as input. In this study, top-of-canopy reflectance images from Sentinel-2 MSI were utilized to derive FAPAR using the biophysical processor. The amount of photosynthetically absorbed radiation (PAR) absorbed by green leaves is known as the fraction of photosynthetically absorbed radiation, or FAPAR. Depending on the source of the incoming radiation, it is a weighted sum of the direct FAPAR and diffuse FAPAR. For each biophysical variable, the processor automatically uses a neural network calibrated and trained over a database simulated by the PROSAIL-5 model. The reflectance in eight spectral bands (B3, B4, B5, B6, B7, B8a, B11, and B12) as well as the cosines of the sun zenith angle, viewing zenith angle, and relative azimuth angle are used in the input layer of neural networks. The output layer provides the linear transfer function, while the tangent sigmoid transfer functions are contained in the hidden layer. The biophysical product was extracted from the reflectance data in a highly effective manner with the help of this trained neural network [38].

(d) Estimation of T_{scalar} (T_s) using MODIS LST (Land surface temperature) Images

MODIS onboard Terra and Aqua satellites offer observations in 36 spectral bands encompassing the visible (459–479 nm, 545–565 nm, 620–670 nm), NIR (841–875 nm, 1230–1250 nm), SWIR (1628–1652 nm, 2105–2155 nm), and TIR bands at a spatial resolution ranging from 250 m to 1 km. A diverse range of observations made by MODIS provides ample opportunity to gather data on temperature stress scalars. In a grid of 1200 × 1220 km, the MOD11A1 V6 product offers daily land surface temperature (LST) and emissivity readings. The MOD11 L2 swath product yields the temperature value. Several satellite data and products are now available through cloud computing resources such as Google Earth Engine (GEE) [39]. As one of the few platforms that readily provides access to freely available long-term data and products, GEE facilitates regional and global studies of spatiotemporal variations of land surface temperature. Thus, using the Google Earth Engine code, the MODIS LST images were retrieved (Table 8). The MODIS-derived LST images from the Google Earth Engine were used to compute T_{scalar} in the ENVI software. Temperature stress parameterizations were made through cardinal temperature-based indices (T_{scalar}), using MODIS MVC surface reflectance at 500 m (MOD09A1) in 841–876 nm and 1628–1652 nm.

$$T_{scalar} = \left(\left(\frac{Tmax - T}{Tmax - Topt}\right) \times \left(\frac{T - Tmin}{Topt - Tmin}\right)\right)\hat{}\left(\frac{Topt - Tmin}{Tmax - Topt}\right)$$

where the value of T_{scalar} ranges between 0 and 1; Tmax stands for the maximum cardinal temperature (28 °C) for wheat growth; Topt is the optimum cardinal temperature (18 °C) for wheat growth; Tmin is the minimum cardinal temperature (5 °C) for wheat growth; and T is the land surface temperature (LST) calculated from the MODIS image.

Table 8. List of MODIS-derived LST images in the Google Earth Engine for calculation of T_{scalar} in ENVI.

S. No.	Rohtak and Jhajjar	Gurugram
1.	26 November 2018	26 November 2018
2.	29 January 2019	5 December 2018
3.	18 March 2019	21 December 2018
4.	3 April 2019	29 January 2019
5.	19 April 2019	23 February 2019
6.		11 March 2019
7.		18 March 2019
8.		3 April 2019

On some days, satellite images were unavailable, and the missing values were interpolated on those days using the equation given below:

$$\mathrm{Ti} = \mathrm{T}_{\mathrm{scalar1}} + \left(\frac{\mathrm{T}_{\mathrm{scalar2}} - \mathrm{T}_{\mathrm{scalar1}}}{\mathrm{T2} - \mathrm{T1}}\right) \times (\mathrm{T} - \mathrm{T}_{\mathrm{scalar1}})$$

where Ti stands for an interpolated value of the missing images for the date between the initial day and final day; $\mathrm{T}_{\mathrm{scalar1}}$ stands for the $\mathrm{T}_{\mathrm{scalar}}$ value on the starting date (initial day); and $\mathrm{T}_{\mathrm{scalar2}}$ stands for the $\mathrm{T}_{\mathrm{scalar}}$ value of the last date (final day).

(e) Estimation of Water Scalar (Ws)

In our study, we used the land surface wetness index (LSWI), which is based on a straightforward approach, to estimate the seasonal dynamics of the water stress scalar (Ws) [37]. The land surface wetness index (LSWI) is a linear combination of SWIR and NIR bands. Water stress parameterization was performed through the land surface wetness index (LSWI) computed in the SNAP toolbox using Sentinel-2 images (Band 8 (NIR) and Band 11 (SWIR)) using the equation stated below:

$$\mathrm{LSWI} = (\rho\mathrm{NIR} - \rho\mathrm{SWIR})/(\rho\mathrm{NIR} + \rho\mathrm{SWIR})$$

where ρNIR stands for reflectance at 800 nm and ρSWIR for reflectance at 1600 nm.

Thus, by using all the values of LSWI, the maximum LSWI value ($\mathrm{LSWI}_{\mathrm{max}}$) was identified from each pixel of the images by coding a program in ENVI software. These LSWI values were further used to obtain water scalar values for all three districts (Rohtak, Jhajjar, and Gurugram), which were calculated in ENVI using the following equation:

$$\mathrm{W_s} = (1 + \mathrm{LSWI})/(1 + \mathrm{LSWI}_{\mathrm{max}})$$

where $\mathrm{LSWI}_{\mathrm{max}}$ stands for maximum LSWI within the wheat growing season for individual pixels.

(f) Estimation of APAR (Absorbed Photosynthetically Active Radiation)

Fraction APAR (FAPAR) was obtained with the help of the SNAP toolbox by processing Sentinel-2A images. The SNAP toolbox is embedded with a global neural net model for deriving FAPAR and LAI from TOC band reflectance values. The NASA Power website obtained global incident radiation for the study area [40]. The following equation was used for calculating APAR:

$$\mathrm{APAR} = \mathrm{FAPAR} \times \mathrm{Rs} \times 0.48 \times \mathrm{T}$$

where FAPAR is the Fraction of Absorbed PAR, Rs is Global Incident Radiation and T is the land surface temperature (LST).

The conversion of APAR into NPP for each time step-1 was established with a temporally variant light use efficiency obtained by reducing ε* by water and temperature stress scalars for each date. Thus, after parameterizations of temperature and water stress, the resampling of imageries to 30 m for Tscalar (Ts) and Wscalar (Ws) images was performed in ENVI. Incident PAR was approximately 48% of incident global solar radiation. The net primary productivity (NPP) was estimated using the equation given below:

$$\mathrm{PP} = \epsilon_{\mathrm{max}} \sum\nolimits_{\mathrm{i}}^{\mathrm{n}} (\mathrm{APAR} \times \mathrm{Ts} \times \mathrm{Ws})$$

where ϵ_{max} stands for maximum radiation use efficiency (RUE). We have used 2.8 as the full RUE for wheat in the study area [41]. For all the estimations, the sowing date for wheat was 15 November 2018. The wheat crop's harvest index (HI) (0.35) was then used to estimate the final predicted yield using the equation below.

$$\mathrm{Grainield} = \mathrm{HI} \times \sum\nolimits_{\mathrm{Sowing}}^{\mathrm{Harvesting}} \mathrm{NPP}$$

By categorizing the multispectral images using a supervised maximum likelihood classifier and employing ground truth training sites, the wheat pixel mask was created independently for OLI and MSI images. All pixels except wheat were masked out in further image analysis, and wheat pixel masks were developed from Landsat 8 and Sentinel-2 imagery.

(g) Evaluation of the Estimated Regional Yield

The methodology has been assessed by comparing the estimated grain yield and the average yield reported during the last five years from the Department of Agriculture and Cooperation (DAC), Ministry of Agriculture and Farmer's Welfare, India. The grain yields have been compared for all three districts at the district level.

2.9. Estimation of Crop Water Productivity (WP) for Winter/Rabi Season 2018–2019

By calculating crop biomass and yield using the harvest index (HI) concept, this study employs crop productivity (kg/m^2) as the numerator and crop consumptive water use (actual seasonal evapotranspiration) as the denominator, both of which were derived from satellite data with ground information input. Thus, after estimating yield and seasonal ET for the three districts, water productivity was calculated in ENVI software for these districts using the following equation:

$$\text{WP} = (\text{Crop productivity})/(\text{Water use})$$

where WP is water productivity (kg/m^3), Crop productivity (kg/m^2 or ton/ha), and Water use is seasonal actual ET (mm, m^3/m^2, or m^3/ha).

The advantages of this method are that the remote sensing method avoids complex land surface processes and biophysical parameter estimations. It does not demand field calibration before new applications and is conveniently transferable. If census production data falls within an appropriate limit, the accuracy looks decent.

3. Results

3.1. Performance of the SETMI Model in the Field Experiment

The performance of the SETMI model was evaluated for sensible heat flux, latent heat flux, and net radiation in maize and wheat crops.

(a) Maize

The SETMI estimated H from the remote sensing images ranged from 96.56 to 205.60 Wm^{-2}, while the scintillometer-measured H went from 96.82 to 217.15 Wm^{-2}. SETMI modeled instantaneous fluxes versus the LAS-measured fluxes for maize crops for years 2015–2016 and 2017–2018 (rainy/*kharif*), indicating good agreement. Results showed a RMSE of 23.92 Wm^{-2} and 8.66 Wm^{-2}, a negative MBE of −8.3 Wm^{-2} and −5.32 Wm^{-2}, and an NRMSE of 16% and 13% (which indicated a slight underestimation) (Figure 6a) for both rainy/*kharif* season experimental years (2015–2016 and 2017–2018), respectively. The coefficient of determination (R^2) of 0.82 indicated less error variance. The H prediction by SETMI was slightly better than the prediction of ET.

In the case of latent heat flux (LE), the SETMI-estimated LE showed good agreement (Figure 6b) with the LAS-estimated LE. Results showed NRMSE values of 14.76% and 14.2%, RMSE values of 33.66 Wm^{-2} and 43.16 Wm^{-2}, and MBE of −19.21 and −29.9, which indicates that the model slightly underestimated the LE and R2 of 0.87 and 0.91 for both experimental years (2015–2016 and 2017–2018), respectively.

Further, ET estimated from the SETMI model and LAS were compared. SETMI predicted ET showed R^2 of 0.98 and 0.89, MBE of 0.40 and 0.48 (i.e., overestimation by model), and NRMSE of 0.244 mm/day (i.e., the error is 24.4%) and 21.6%, thus indicating reasonably good model performance (Figure 6c).

Ground observation of net radiation was compared with net radiation obtained from the SETMI model. The model estimated Rn (Figure 6d) within an error of 13.9% relative to measured Rn using net radiometers. This was comparable to other published studies [42,43],

where Rn was predicted to have an associated error of about 10%. With an RMSE value of 38.10 Wm^{-2} and 31.32 Wm^{-2} and an NRMSE of 9% and 19% for both experimental years (2015–2016 and 2017–2018), respectively, in the model, the predicted Rn was calculated, which shows excellent correspondence of the model with scintillometer measurements. Considering the percentages of the RMSE to the corresponding measurement means, the results indicate that the SETMI performed adequately well for maize, within the typical measurement errors of scintillometer systems.

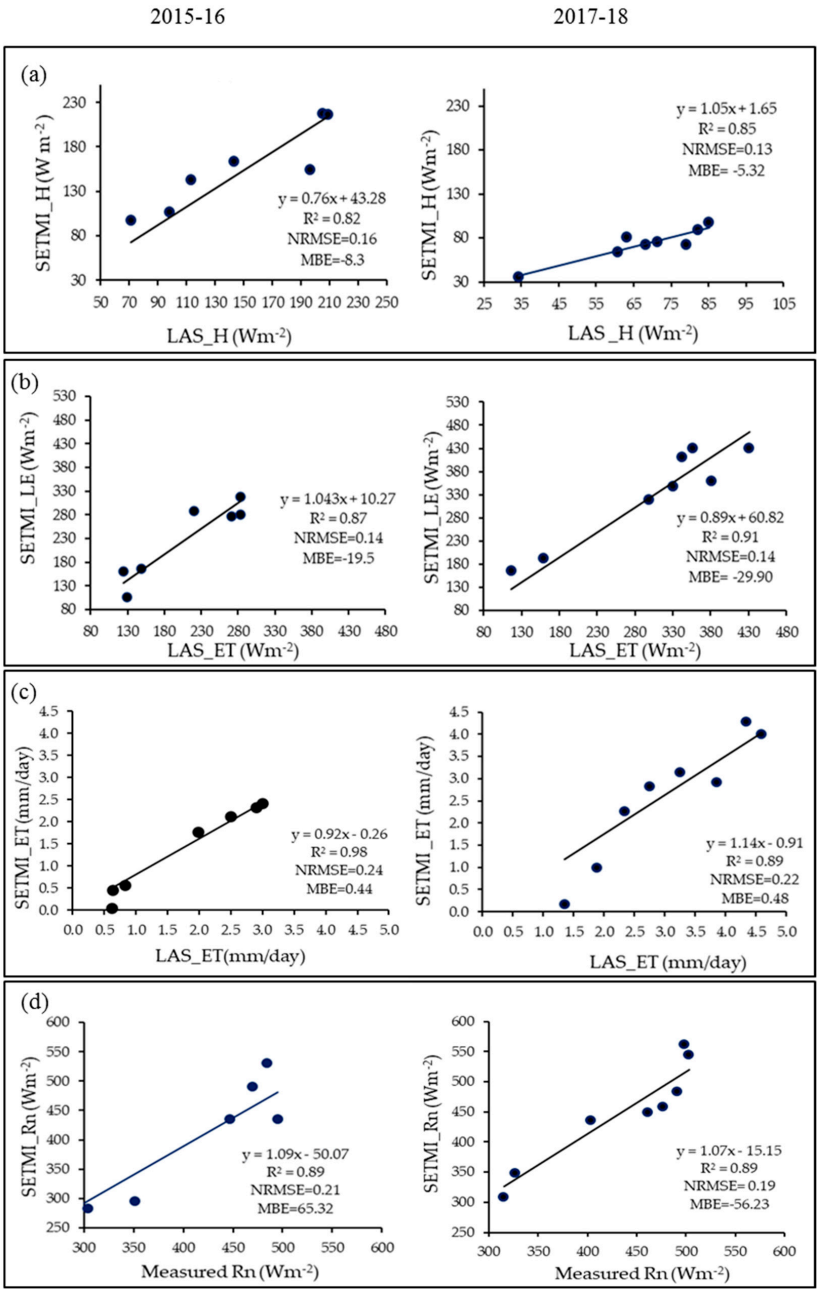

Figure 6. Validation of the SETMI model using measurements for (**a**) sensible heat flux, (**b**) latent heat flux, (**c**) evapotranspiration, and (**d**) net radiation across the rainy seasons of 2015–2016 and 2017–2018 in maize.

(b) Wheat

The SETMI estimated sensible heat flux (H) (Figure 7a) showed good correspondence with measured H by scintillometer, with a value of NRMSE of 29% and 22%, RMSE value as 26.45 Wm^{-2} and 24.05 Wm^{-2}, R^2 as 0.95 and 0.86, and MBE as −25.82 and −5.78 (indicating

underestimation by the SETMI model) for the years 2015–2016 and 2016–2017, respectively. For LE, NRMSE was observed to be 8% and 23%, RMSE as 12.57 Wm^{-2} and 61.74 Wm^{-2}, MBE as 6.78 Wm^{-2} and −56.59 Wm^{-2} and R^2 as 0.92 and 0.95 for the experimental years 2015–2016 and 2016–2017, respectively (Figure 7b). In the case of ET (mm/day) (Figure 7c), R^2 was observed as 0.98 and 0.86, NRMSE as 28%, RMSE as 0.29 mm/day and 0.52 mm/day, and MBE as 0.26 and 0.41 (the positive MBE values show the model slightly overestimated ET) in both experimental years 2015–2016 and 2016–2017, respectively. The result indicated that SETMI estimated net radiation (Rn) agreed with in-situ measured Rn (Figure 7d), with the NRMSE value being 14% and 12%, the RMSE as 37.56 Wm^{-2} and 46.17 Wm^{-2}, and the MBE as 24.22 and −30.13. The R^2 values are 0.90 and 0.83, representing less variance in error.

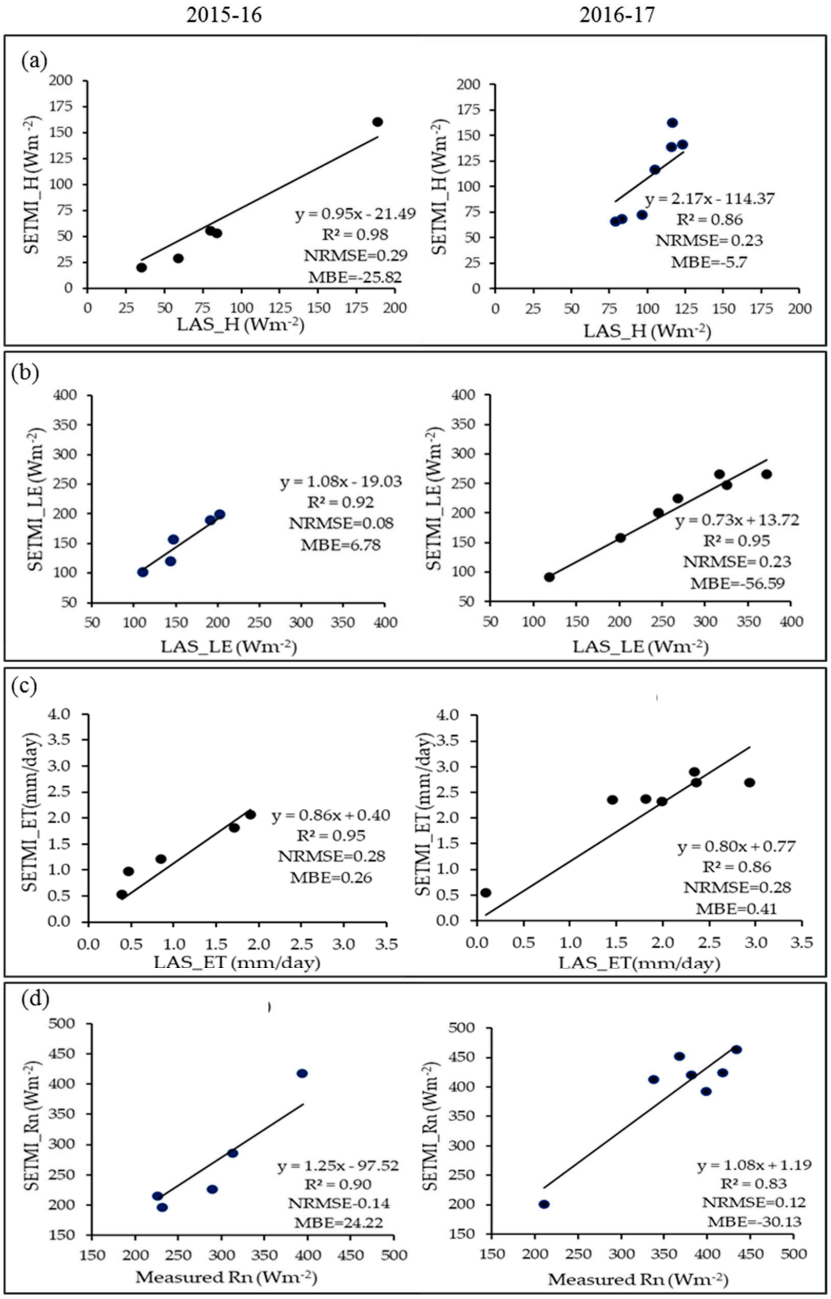

Figure 7. Validation of the SETMI model using measurements for (**a**) sensible heat flux, (**b**) latent heat flux, (**c**) evapotranspiration, and (**d**) net radiation across the winter seasons of 2015–2016 and 2016–2017 in wheat.

3.2. Estimation of Regional Wheat Water Productivity

3.2.1. Regional Actual Evapotranspiration Using the SETMI Model

Actual seasonal ET for the wheat crop was calculated for three districts (Rohtak, Jhajjar, and Gurugram) of Haryana (northwestern region of India) in the year 2018–2019 (November 2018 to April 2019). It revealed significant spatial variation in these districts (Figure 8). The estimated seasonal actual ET ranged from 101 mm to 325 mm for the wheat in the study area. The overall spatial patterns in seasonal ETa distribution in the winter (*rabi*) season show a strikingly uneven distribution of water use by wheat among the districts. Most areas in Rohtak and Jhajjar showed lower actual ET (101–130 mm), while areas in Gurugram fdistrict showed relatively greater actual ET (221–295 mm). Many areas in yellow (mainly in the northern areas of the district) showed high ET in the range of 311 to 325 mm, which may be due to sufficient irrigation, leading to excellent wheat growth conditions. The non-cropped areas, mostly settled areas of cities, are depicted in red. In areas with lower seasonal ETa, the wheat might have experienced water stress during the season.

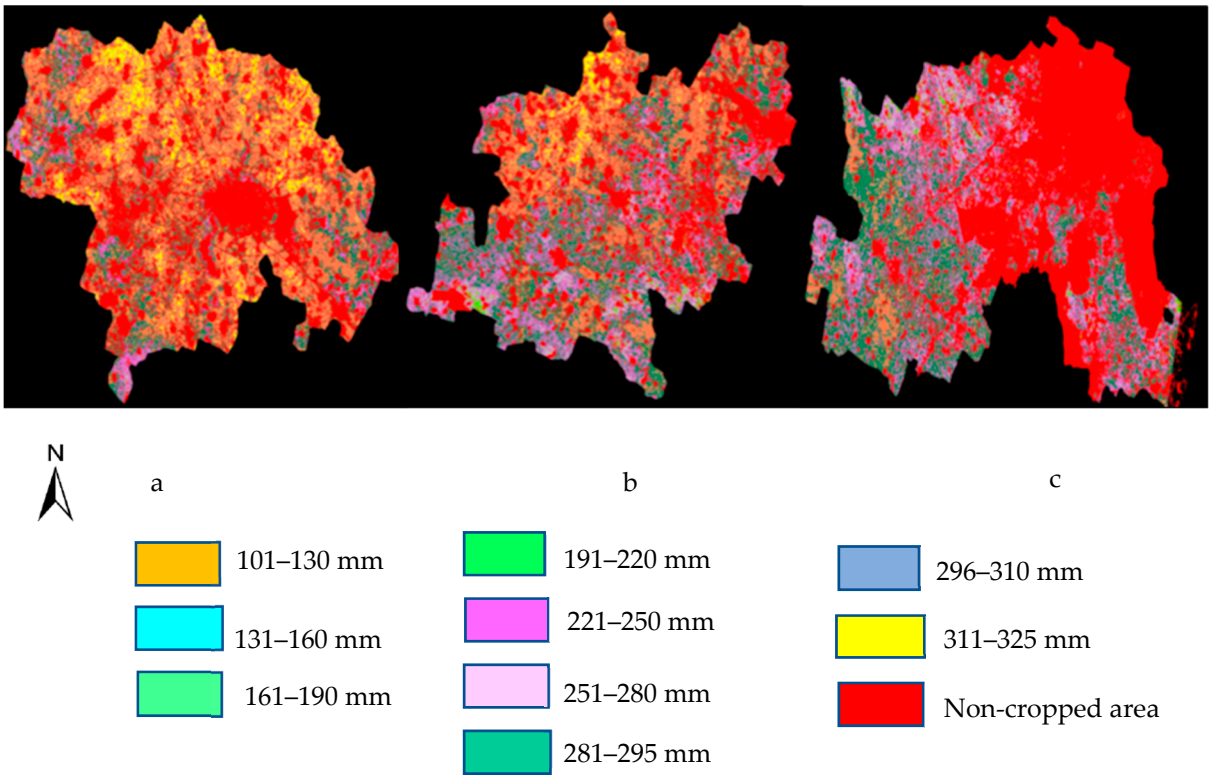

Figure 8. Seasonal actual ET map (November–April 2018–2019) of (**a**) Rohtak, (**b**) Jhajjar, and (**c**) Gurugram districts by applying the SETMI model for the wheat crop grown in the winter/*rabi* season (2018–2019).

The southwestern part of the Jhajjar district depicts above-average ET, indicating wheat growth flourished in this area.

3.2.2. Regional Wheat Yield Estimation for Winter/Rabi Season (2018–2019)

Accurate wheat yield mapping in different parts of the study regions is very critical because of its importance for spatially computing crop water productivity. The district-wise estimated grain yield ranged from 2 t ha^{-1} to 6 t ha^{-1} (Figure 9). In most areas in Jhajjar, the yield ranged from 4 t ha^{-1} to 6 t ha^{-1}, with a small proportion of the wheat field distributed across the district exhibiting a yield range of 2 t ha^{-1} to 4 t ha^{-1}. Like Jhajjar, Rohtak yields ranged from 4 t ha^{-1} to 6 t ha^{-1}. The non-cropped areas are depicted in white. In the case of Gurugram, the higher wheat yield area is mainly concentrated in the western, southern,

and south-eastern regions, with green shade dominating all these regions. Thus, it was observed that the Jhajjar district showed the maximum yield, followed by Rohtak, and the least yield (t/ha) was observed in the case of Gurugram. Yields agreed with the past years' yield statistics of DAC, Ministry of Agriculture and Farmers Welfare, India, for Rohtak, Jhajjar, and Gurugram districts. The area under wheat cultivation was highest in Jhajjar, followed by Rohtak, and the least under wheat cultivation was in Gurugram. The wheat yields also followed a similar pattern to the cultivated wheat area.

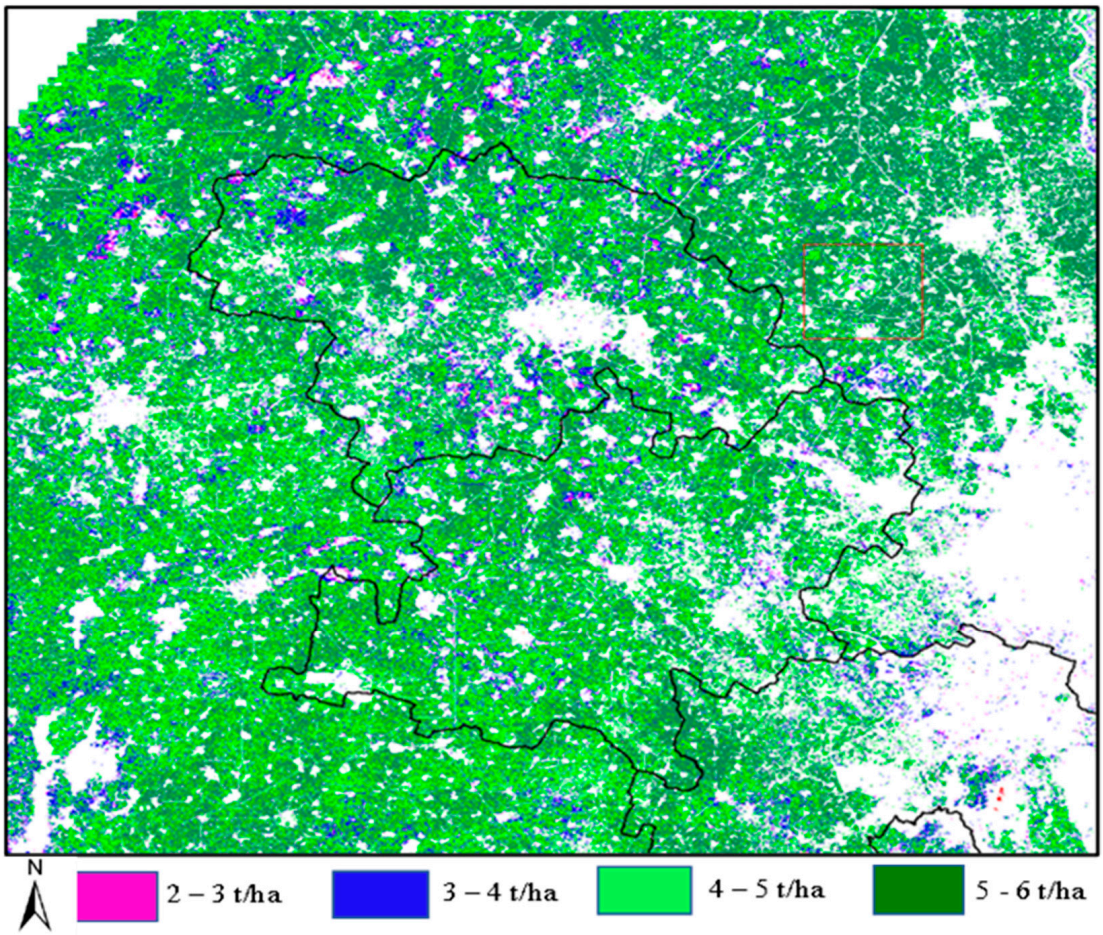

Figure 9. Spatial distribution of wheat yield (t/ha) using the PEM approach for three study districts (indicated by black boundary lines) of Rohtak, Jhajjar, and Gurugram for 2018–2019.

3.2.3. Regional Wheat Water Productivity for the Winter/Rabi Season (2018–2019)

After calculating the spatial yield and seasonal actual ET for the three study districts, maps of wheat water productivity for the districts were generated (Figure 10a–c). In the case of Rohtak, cyan color (2.1 kg m^{-3}–2.3 kg m^{-3}) dominated more than 50% of the pixels, followed by light green color (1.8 kg m^{-3}–2 kg m^{-3}). Few clusters in the northwestern region of the district show a prevalence of red and yellow colors. This region indicated low WP (0.9 kg m^{-3}–1.5 kg m^{-3}). The non-cropped areas are represented by black color. Continuous fields of high WP were perceived in the northeast of the district. Regions of very low WP (0–0.9 kg m^{-3}) denoted in red indicate the presence of feeble crop growth, disease, soil salinity, or water bodies. In the case of Jhajjar, the prominence of cyan-colored pixels (>80%) can be seen throughout the region. This reflects that water productivity in these areas remained between 2.0 kg m^{-3} and 2.25 kg m^{-3}. This was followed by yellow and light green pixels, especially in southern regions, indicating that wheat water productivity was between 1.5 kg m^{-3} and 2.0 kg m^{-3}. Looking at the spatial distribution of wheat water productivity in Jhajjar district, it can be said that there is more uniformity in distribution

than in Rohtak district. Non-cropped areas were represented by black, and pixels near these black areas showed the lowest water productivity, denoted by red (0–0.9 kg m^{-3}).

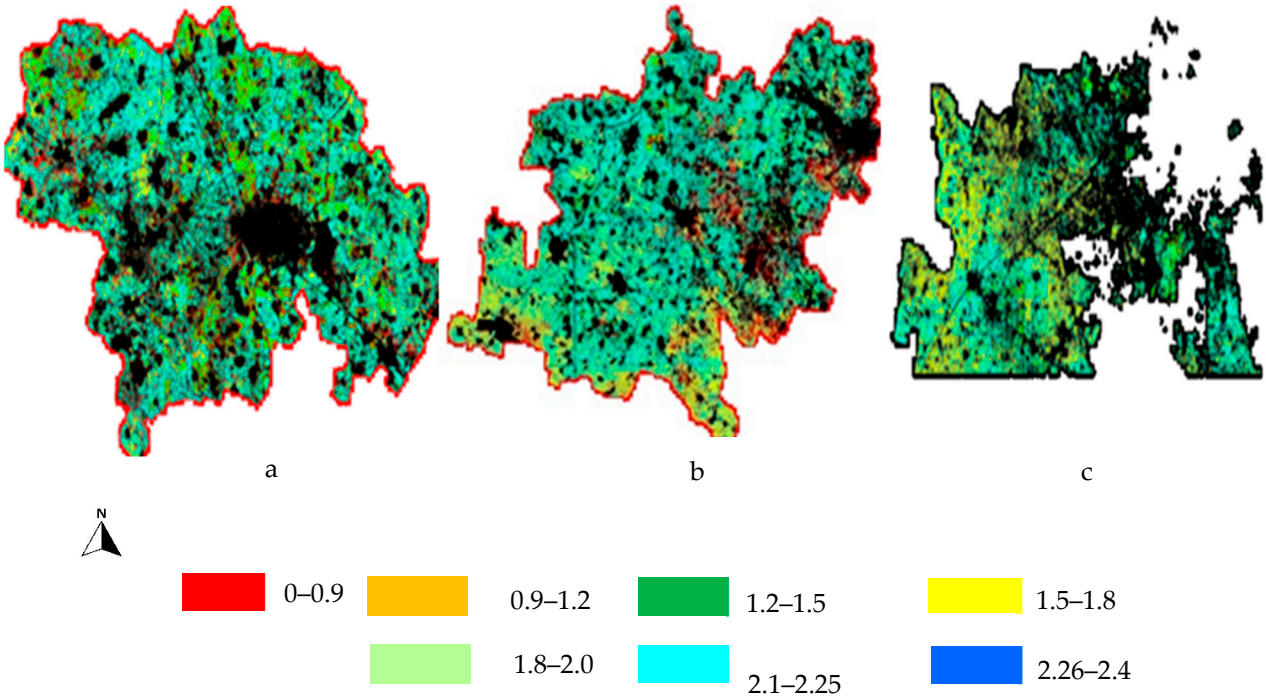

Figure 10. Spatial distribution of water productivity (kg mm^{-3}) of the wheat crop in the *Rabi* season of the year 2018–2019 for (**a**) Rohtak, (**b**) Jhajjar, and (**c**) Gurugram districts.

In the case of Gurugram, the spatial distribution of wheat water productivity showed the slightest variation among the three districts, with a range restricted to yellow (1.5 kg m^{-3}–1.8 kg m^{-3}), light green (1.8 kg m^{-3}–2.0 kg m^{-3}) and cyan color (2.01 kg m^{-3}–2.25 kg m^{-3}). Therefore, an average WP with high variability was observed for the wheat crop. Due to scanty rainfall patterns, wheat depends on groundwater; hence, it is mainly produced under irrigated conditions. Also, among all three districts, the least water productivity was observed in the case of Gurugram (2018–2019), with more areas having WP ranging between 1.5 kg m^{-3} and 2.0 kg m^{-3}. In contrast, Jhajjar and Rohtak showed a near-similar spatial distribution of water productivity.

4. Discussion

Developing nations with agriculture-based economies and fast-growing populations require quick and reliable estimations of ET to aid with irrigation scheduling and improve agricultural water yield. From our study, it can be inferred from the results that SETMI overestimated daily ET (mm/day) (as evident from MBE) in maize crops in the rainy/*kharif* season of both experimental years (2015–2016 and 2017–2018). This slight overestimation might be due to differences in maize crop condition at various stages due to differences in crop sowing dates and harvesting times, leading to different types of patches in the field (non-uniformity in the field over a larger path length). It included patches where a crop had already been harvested, residues were somewhere, small patches were where still-standing mature crops were, and patches where bare soil existed. Various factors might cause a low ET area in the field. Crop coefficient patterns may aid in identifying sites with early senescence or slowed growth. Low ET might be caused by crop health issues or water stress. Identifying these locations may improve management methods, including purposely applying more irrigation in low ET zones. Similarly, the SETMI model overestimated Rn in both experimental years (2015–2016 and 2017–2018) for maize crops. In the case of LE and H, a slight underestimation was observed by the SETMI model in

both rainy/*kharif* seasons of the maize crop, which may be attributed to heterogeneity developed due to different dates of irrigation, which led to additional surface wetness and biomass development along the scintillometer pathlength. This resulted in inconsistent surface conditions with those captured by remote sensing pixels. This could, therefore, explain to some extent the differences in the remote sensing-based H and the LAS observed. H. Barker et al. [30], in their work for irrigation management using the SETMI model, observed that the model seems to predict Rn effectively for all image dates but tends to underestimate H and overestimate G and LE usually. However, in their cotton investigation, Neale et al. [44] showed more significant agreement for all fluxes, with an underestimation of H of considerably less significance; they observed good agreement with LE.

For wheat crops, SETMI underestimated sensible heat flux (H) in the winter/*rabi* season in both experimental years (2015–2016 and 2016–2017). However, ET and LE were overestimated by the SETMI model, as shown in the reported values. In their research, Geli et al. [45] demonstrated applying the hybrid ET model to rainfed wheat, a common crop in Mediterranean settings. The flux model corresponded with the experiment's observed fluxes and ET values. The six satellite images yielded RMSE = 0.33 mm day^{-1} in ET and 32 Wm^{-2} in LE. The net radiation was overestimated in 2015–16 but underestimated in 2016–2017. So, no clear pattern was detectable in the case of net radiation estimation by the SETMI model. The model needs to be further studied and researched to be used and applied in local areas of Indian regions. Bispo et al. [46], in their study, found that the modeled energy balance components had a significant connection to the ground data from EC, with ET showing an R^2 of 0.94 and a Pearson correlation coefficient (r) of 0.88. In Brazil, the average collected ETa was 1025 mm, yielding ETa rates of 2.9 mm per day across two seasons in tropical climates to improve irrigation management in the sugarcane crop. They concluded that the SETMI hybrid model generated appropriate estimated daily ETa values through the TSEB model during the evaluated growing periods, affirming the model's potential application in tropical environments in Brazil. The model generally overestimated Rn and ET values but underestimated instantaneous LE and H fluxes. Typically, for all the parameters across the seasons, a very high R^2 (0.83–0.95) and average error ranging between 8% and 29% in model estimation indicate a reasonably good performance of the model and the physics behind the SETMI model.

The sources of yield, ET, and WP differences can be identified by investigating the internal (genetic) and external (environmental) elements that influence crop output. Seasonal ET estimations of selected regions using the SETMI model showed decent results. The overall spatial variations in seasonal Eta (winter/rabi, 2018–19) demonstrate a remarkably unequal water distribution in the Rohtak district. Many of the areas had actual ET ranging from 101 to 130 mm. The northern part of the district exhibited high ET in the 311 to 325 mm range, which might result from favorable growing conditions and, consequently, abundant crop growth. The bulk of actual evapotranspiration was seen to be in the upper and lower categories, as yellow and orange colors were predominant; however, 281–295 mm (green) Eta was also discovered in a few areas. These area pixels are primarily concentrated in the district's eastern, southern, and north-western regions. For wheat crop cultivation, the optimal irrigation requirement is 60 mm of water at five critical crop growth stages (generally, the irrigation requirement of wheat is 300 mm to 350 mm over the season). So, it is expected that the seasonal Eta for the wheat season should be much lower than 300 mm. The spatial distribution indicated that, despite providing irrigation, crops suffered water stress during the winter/*rabi* season 2018–2019 in areas that showed ETa below 220 mm. Though the district has a dense canal network, the network is exceptionally substantial in the center and south of the district. However, the district suffers from water logging and soil salinity issues in the canal regions, which might have affected crop growth. Water and salt stress are known to lower the ETa in the field. Being difficult under field conditions, ET measurement is thus uncommon in the Rohtak, Jhajjar, and Gurugram districts.

Generally, seasonal ETa distribution patterns showed a remarkable inconsistency in water distribution in wheat-growing areas. Most district regions are green (281–295 mm),

indicating above-average ETa levels. Furthermore, several places displayed pink shades, indicating ET in the optimum range (221–280 mm). Several regions had an orange hue, showing areas of lower ET. So, these areas experienced water stress or poor crop growth, possibly due to soil salinity, disease, or other issues. Water consumption (actual ET) is variable, and high ET is not always associated with high yield or WP. Better water management procedures are required to prevent needless ET, such as evaporation from saline regions. The southern section of the Jhajjar district showed above-average ET, indicating that wheat crops thrived well in this location. The yellow ETa class on the maps reflects exceptionally high ETa regions (311–325 mm), suggesting either the over-application of irrigation water or robust crop growth.

Furthermore, the spatial map of Gurugram exhibited less spatial variability for ETa. The district is characterized by ETa in predominantly green-class cropped areas, with ET ranging from 281 mm to 295 mm. High actual ETa areas (311–325 mm) of yellow color class are barely identifiable in the Gurugram district, unlike Jhajjar and Rohtak, which indicated less variability in the spatial distribution of actual ET. Because of the water on the ground surface, basin irrigation has high evaporation rates. Chukkalla et al. [47] presented a summary of ET savings techniques. Furrow and border irrigation saturate the soil sporadically, causing soil evaporation during soaking episodes and a ponded surface towards the field's tail end. Thus, the type of irrigation also influences the actual ET estimates. Our study used the districts' basin irrigation to model ET estimates, which may only be accurate for some locations. Using Landsat 8 images and the SEBAL model to forecast radiative fluxes and daily ET distribution, Silva et al. [48] and Beg et al. [49] identified comparable patterns. Thus, even within the homogenous wheat crop state, ET rates exhibited an extensive range of variance. Doorenbos and Kassam [50] stated that the ET for wheat ranged from 450 to 650 mm. Bastiaanssen et al. [51] calculated a mean ET of 360 mm with a standard variation of 15 mm across wheat regions in the Sirsa district (Nov.–Apr. 2002) using the SEBAL model. Wheat yields depend more on irrigation volume than precipitation, river flows, or soil moisture content. This reveals why wheat yields in the Indian states of Haryana and Punjab are so high since considerable irrigation is used in these areas, accompanied by significant groundwater overexploitation. Wheat yield and WP follow the ET trend more closely.

During the yield mapping of wheat crops in Jhajjar, wheat crops covered most of the region, unlike Gurugram. The area under wheat cultivation was highest in the case of Jhajjar, followed by Rohtak, and the most minor area under wheat cultivation was in Gurugram. Most of the pixels showed higher yield values compared to Gurugram. This indicates that better crop management practices were followed in Jhajjar. In Rohtak, wheat yields mainly varied from 4 t ha^{-1} to 6 t ha^{-1}, like in Jhajjar. Gurugram's wheat crop was primarily concentrated in the western, southern, and southeastern sections, and it showed the least crop productivity [52]. Wheat crops respond well to appropriate irrigation but cannot sustain excessive watering. On the other hand, water stress may harm crop yield during the crop's 'critical growth period'. Furthermore, climate change is causing excessive heat and water shortages, resulting in increased soil moisture stress and evapotranspiration, increasing the requirement for irrigation throughout the summer and winter/*rabi* seasons. The WP appears to vary within the irrigation system and significantly between fields. This suggests that, in addition to climatology and regional soil characteristics and hydrological constraints, farm management factors such as irrigation amount and timing, fertilization, weeding, seed variety selection, crop rotation, and so on serve a significant role in the WP attained. Lobell et al. [53] concluded that management variables were more relevant than soil type and climatic changes in Yaqui Valley wheat yield spatial variability. Overall, the Jhajjar region had the highest yield due to the higher area under cultivation. Wheat yields were assessed in 24 farmer plots in the Sirsa district of Haryana state during the 2001–2002 winter/*rabi* season by Van Dam et al. [54]. The average measured yield was 4.6 t ha^{-1} (σ~1.3), but SEBAL estimated yields were somewhat lower at 4.0 t ha^{-1} (σ~0.8). But this low estimate could be due to the coarser resolution of the satellite used, unlike in our study,

where we used Sentinel-2A with better resolution, which could better identify small and individual fields.

Water productivity (WP) was computed for the three districts after yield and seasonal actual ET were obtained. In the case of Rohtak, regions of very low WP (0–9 kg m^{-3}) denoted by red color indicate the presence of either feeble crop growth or disease or soil salinity or the presence of water bodies or poor soil health or poor crop management practices. This low WP patch clues into the status of other underperforming sections that comprise an essential part of the district. In the district of Jhajjar, the presence of cyan-colored pixels (>80%) can be detected across the areas, with water productivity in these locations varying between 2.0 kg m^{-3} and 2.25 kg m^{-3} range followed by yellow and light green pixels (1.5 kg m^{-3} to 2.0 kg m^{-3}), particularly in the south. However, greater homogeneity was observed in the Rohtak district. Water productivity variations may be linked to various reasons, including water deficit, soil salinity, crop density, field leveling, weeds, water logging, and soil moisture. In Gurugram, the spatial distribution of wheat water productivity exhibited the least variance among the three districts. Wheat is mainly produced as an irrigated crop due to the scanty rainfall scenario prevailing in the winter/*rabi* season and thus is dependent on canal irrigation and groundwater. The current national average water productivity of wheat was estimated to be 1.06 kg m^{-3} [55], 0.8–1.0 kg m^{-3} [56], and ranging between 0.62 and 1.1 kg m^{-3} in northwestern India, depending on nitrogen application and wheat variety grown [57]. Among all the three districts, the least water productivity was observed in the case of Gurugram (winter/*rabi* 2018–2019), with more areas having WP ranging between 1.5 kg m^{-3} and 2.0 kg m^{-3}. Hussain et al. [58] calculated a WP value of 1.36 kg m^{-3} for wheat in Haryana. Singh et al. [59] reported that in the Sirsa district of Haryana, the average WP at the selected farms was 1.39 kg m^{-3} for wheat and displayed average values for the meteorological and growing circumstances in northwest India. Sharma et al. [23] reported an average water productivity of 1.57 kg m^{-3} for wheat in Haryana. Our study found much scope for improving WP's full potential in all three districts. It should be considered that the findings discovered in the literature are not only related to methodological variances, scale of measurements, weather variables, and year of measurement but also vary, resulting in a complication of comparison. Also, the WP values are influenced by both yield and ET. The WP values increase as the yield increases, so the main issue would be to enhance yield. While yield increases often take years, another method for improving WP simultaneously would be to lower ET by increasing the efficacy of water application or optimizing other agronomic practices. The availability of heavily subsidized water, power, and fertilizers results in ineffective water usage, highlighting the requirement to shift away from input subsidies and toward direct benefit distribution to farmers, depending on the field area. Increased water prices must be synchronized with better and more timely water supply so that surface irrigation's operation and maintenance costs are entirely repaid. Other methods of improving water productivity involve enhancing the irrigation efficiency of both canal and groundwater irrigation by including precision irrigation technologies such as micro-irrigation. Also, locations with low yields (<3 t ha^{-1}) show more significant variations in WP values, suggesting larger variability in water usage despite equal yields.

Certain limitations to estimating regional water productivity include the availability of quality ground data and frequent satellite imagery of the region. Census statistics are obtained using a labor-intensive approach, leading to inaccuracies and skewed values. Many steps, such as sensor calibration and atmospheric/topographic correction, are required to transform remote sensing data to ground values, during which errors may remain. Crop growth is inextricably connected to land, crops, and water management techniques, so there is plenty of room for improvement. Under these conditions, it is essential to persuade farmers to implement cutting-edge solutions, like laser field leveling and bed furrow irrigation systems, which might save significant water. Better management and intelligent fertilizer application to the wheat crop, which accounts for around 35.2% of total wheat crop spending, might be economically beneficial and improve crop growth

and, thus, WP [57]. A more significant challenge in using the SETMI model for practical applications is the availability of cloud-free satellite images, especially during rainy/*kharif* season in India. The availability of better-resolution thermal images from future satellite missions, like TRISHNA (Thermal infraRed Imaging Satellite for High-resolution Natural Resource Assessment), will provide additional opportunities to develop better local water management applications using surface energy balance models. As a result, future research will concentrate on model parameterization and using aerial and satellite images from other sensors to enhance image frequency. Also, results from the implementation of a large aperture scintillometer (LAS) may improve our understanding of how spatial model estimates of fluxes compare, or at the very least provide hints of the related level of variability, and it encourages future implementations of scintillometers to validate spatial estimates of surface energy balance models. A fundamental aim that has yet to be fulfilled is transforming remotely sensed images into quantitative water consumption knowledge at scales significant to water management organizations. This study is one such step in that direction.

5. Conclusions

A research study was conducted to estimate crop evapotranspiration using a large aperture scintillometer (LAS) and the Spatially ET Mapping Interface (SETMI) model in a semi-arid region of India for irrigated wheat and maize crops. This validated SETMI model was then used to estimate regional wheat water productivity using Landsat 8 and Sentinel-2A imageries of the northwestern semi-arid region of India. For different fluxes across the seasons by SETMI, a very high R^2 (0.83 to 0.95) and NRMSE ranging between 8% and 29% for LAS measurements indicate a reasonably good performance of the model and the physics embedded in the SETMI model. Overall, the SETMI model performed better in the case of the maize crop (rainy/*kharif*) than in the case of the wheat crop (winter/*rabi*). Crop fields may be identified and contrasted owing to the precise prediction of yield and ET values with enough spatial resolution to represent crop-field heterogeneity. The seasonal actual ET mainly ranged between 101 mm and 325 mm in all three districts. Wheat water productivity varied greatly, ranging from 0.9 kg m^{-3} to 2.20 kg m^{-3} in the three districts with low levels of water productivity. This provides an excellent opportunity for effective water usage and increased output in these areas. Jhajjar, which had a high crop productivity value, also had a high level of WP. However, with micro-irrigation, such as sprinkler irrigation in these districts, there is more potential for saving limited water resources and thereby sustainably enhancing productivity and profitability in low crop and water productivity areas. Since Indian agriculture is susceptible to droughts, the frequency and severity of which are expected to rise with climate change, there is a responsibility to make the most significant use of the country's limited water resources.

Author Contributions: Conceptualization, V.K.S.; methodology, V.K.S. and P.S.; software, V.K.S. and C.M.U.N.; validation, V.K.S., R.D., C.M.U.N. and I.Z.G.; formal analysis, V.K.S. and P.S.; investigation, P.S. and V.K.S.; resources, V.K.S., D.K.D., J.M. and M.K.; data curation, P.S. and V.K.S.; writing—original draft preparation, P.S.; writing—review and editing, P.S., V.K.S., A.R., R.D., P.K.J. and S.K.D.; visualization, P.S., V.K.S. and P.K.J.; supervision, V.K.S., C.M.U.N. and R.D. All authors have read and agreed to the published version of the manuscript.

Funding: This research received no external funding.

Data Availability Statement: Data will be made available on request.

Acknowledgments: This work has been conducted as collaborative research between the ICAR-Indian Agricultural Research Institute (ICAR-IARI), New Delhi, and the Daugherty Water for Food Global Institute at the University of Nebraska, USA. The authors would also like to thank the anonymous reviewers for their insightful comments, which helped us enhance the paper.

Conflicts of Interest: The authors declare that there are no conflicts of interest, either financial or otherwise.

References

1. Kirda, C.; Kanber, R. Water, no longer a plentiful resource, should be used sparingly in irrigated agriculture. In *Crop Yield Response to Deficit Irrigation*; Kluwer Academic Publishers: Dordrecht, The Netherlands, 1999; pp. 1–20.
2. Morante-Carballo, F.; Montalván-Burbano, N.; Quiñonez-Barzola, X.; Jaya-Montalvo, M.; Carrión-Mero, P. What do we know about water scarcity in semi-arid zones? A global analysis and research trends. *Water* **2022**, *14*, 2685. [CrossRef]
3. Karimi, P.; Bastiaanssen, W.G. Spatial evapotranspiration, rainfall and land use data in water accounting–Part 1: Review of the accuracy of the remote sensing data. *Hydrol. Earth Syst. Sci.* **2015**, *19*, 507–532. [CrossRef]
4. Abdollahnejad, A.; Panagiotidis, D.; Surový, P. Estimation and extrapolation of tree parameters using spectral correlation between UAV and Pléiades data. *Forests* **2018**, *9*, 85. [CrossRef]
5. Gu, L.; Meyers, T.; Pallardy, S.G.; Hanson, P.J.; Yang, B.; Heuer, M.; Hosman, K.P.; Riggs, J.S.; Sluss, D.; Wullschleger, S.D. Direct and indirect effects of atmospheric conditions and soil moisture on surface energy partitioning revealed by a prolonged drought at a temperate forest site. *J. Geophys. Res. Atmos.* **2006**, *111*, D16102. [CrossRef]
6. Gdoutos, E.E. Fundamentals of Optics. In *Experimental Mechanics: An Introduction*; Springer International Publishing: Cham, Switzerland, 2021; pp. 19–69.
7. Lagouarde, J.P.; Jacob, F.; Gu, X.F.; Olioso, A.; Bonnefond, J.M.; Kerr, Y.; Mcaneney, K.J.; Irvine, M. Spatialization of sensible heat flux over a heterogeneous landscape. *Agronomie* **2002**, *22*, 627–633. [CrossRef]
8. Xue, J.; Bali, K.M.; Light, S.; Hessels, T.; Kisekka, I. Evaluation of remote sensing-based evapotranspiration models against surface renewal in almonds, tomatoes and maize. *Agric. Water Manag.* **2020**, *238*, 106228. [CrossRef]
9. Jin, Z.; Azzari, G.; You, C.; Di Tommaso, S.; Aston, S.; Burke, M.; Lobell, D.B. Smallholder maize area and yield mapping at national scales with Google Earth Engine. *Remote Sens. Environ.* **2019**, *228*, 115–128. [CrossRef]
10. Gowda, P.H.; Chavez, J.L.; Colaizzi, P.D.; Evett, S.R.; Howell, T.A.; Tolk, J.A. ET mapping for agricultural water management: Present status and challenges. *Irrig. Sci.* **2008**, *26*, 223–237. [CrossRef]
11. Glenn, E.P.; Nagler, P.L.; Huete, A.R. Vegetation index methods for estimating evapotranspiration by remote sensing. *Surv. Geophys.* **2010**, *31*, 531–555. [CrossRef]
12. Kalma, J.D.; McVicar, T.R.; McCabe, M.F. Estimating land surface evaporation: A review of methods using remotely sensed surface temperature data. *Surv. Geophys.* **2008**, *29*, 421–469. [CrossRef]
13. Bastiaanssen, W.G. *Regionalization of Surface Flux Densities and Moisture Indicators in Composite Terrain: A Remote Sensing Approach under Clear Skies in Mediterranean Climates*; Wageningen University and Research: Wageningen, The Netherlands, 1995.
14. Bastiaanssen, W.G.; Menenti, M.; Feddes, R.A.; Holtslag, A.A. A remote sensing surface energy balance algorithm for land (SEBAL). 1. Formulation. *J. Hydrol.* **1998**, *212*, 198–212. [CrossRef]
15. Su, Z. The Surface Energy Balance System (SEBS) for estimation of turbulent heat fluxes. *Hydrol. Earth Syst. Sci.* **2002**, *6*, 85–100. [CrossRef]
16. Allen, R.G.; Tasumi, M.; Trezza, R. Satellite-based energy balance for mapping evapotranspiration with internalized calibration (METRIC)—Model. *J. Irrig. Drain. Eng.* **2007**, *133*, 380–394. [CrossRef]
17. Senay, G.B.; Bohms, S.; Singh, R.K.; Gowda, P.H.; Velpuri, N.M.; Alemu, H.; Verdin, J.P. Operational evapotranspiration mapping using remote sensing and weather datasets: A new parameterization for the SSEB approach. *J. Am. Water Resour. Assoc.* **2013**, *49*, 577–591. [CrossRef]
18. Singh, R.K.; Senay, G.B.; Velpuri, N.M.; Bohms, S.; Scott, R.L.; Verdin, J.P. Actual evapotranspiration (water use) assessment of the Colorado River Basin at the Landsat resolution using the operational simplified surface energy balance model. *Remote Sens.* **2013**, *6*, 233–256. [CrossRef]
19. Long, D.; Singh, V.P. A two-source trapezoid model for evapotranspiration (TTME) from satellite imagery. *Remote Sens. Environ.* **2012**, *121*, 370–388. [CrossRef]
20. Norman, J.M.; Kustas, W.P.; Humes, K.S. Source approach for estimating soil and vegetation energy fluxes in observations of directional radiometric surface temperature. *Agric. For. Meteorol.* **1995**, *7*, 263–293. [CrossRef]
21. Brauman, K.A.; Siebert, S.; Foley, J.A. Improvements in crop water productivity increase water sustainability and food security—A global analysis. *Environ. Res. Lett.* **2013**, *8*, 024030. [CrossRef]
22. Pulido-Velazquez, M. Beyond Crop Per Drop: Assessing Agricultural Water Productivity and Efficiency in a Maturing Water Economy. *Water Econ. Policy* **2020**, *6*, 1980005. [CrossRef]
23. Sharma, B.R.; Gulati, A.; Mohan, G.; Manchanda, S.; Ray, I.; Amarasinghe, U. Water Productivity Mapping of Major Indian Crops. 2018. Available online: https://www.nabard.org/auth/writereaddata/tender/1806181128Water%20Productivity%20Mapping%20of%20Major%20Indian%20Crops,%20Web%20Version%20(Low%20Resolution%20PDF).pdf (accessed on 25 April 2019).
24. Sadras, V.O.; Angus, J.F. Benchmarking water-use efficiency of rainfed wheat in dry environments. *Aust. J. Agric. Res.* **2006**, *57*, 847–856. [CrossRef]
25. Pal, O.; Hemraj, S.S. Flash-Flood Potential Mapping in Agricultural Land Using Rule-Based Classification Approach on Multi-Temporal Synthetic-Aperture Radar (SAR) Data over Jhajjar and Rohtak Districts of Haryana State. *South Asian J. Eng. Technol.* **2022**, *4*, 160–165. [CrossRef]
26. Yadav, V. Vulnerability of A District: A Case of Rohtak, Haryana. *Space* **2013**, *17*, 93–101.
27. Chaudhary, B.S.; Saroha, G.P.; Yadav, M. Human induced land use/land cover changes in northern part of Gurgaon district, Haryana, India: Natural resources census concept. *J. Hum. Ecol.* **2008**, *23*, 243–252. [CrossRef]

28. Maguire, M.S.; Neale, C.M.; Woldt, W.E.; Heeren, D.M. Managing spatial irrigation using remote-sensing-based evapotranspiration and soil water adaptive control model. *Agric. Water Manag.* **2022**, *272*, 107838. [CrossRef]
29. Geli, H.M.; Neale, C.M. Spatial evapotranspiration modelling interface (SETMI). In *Remote Sensing and Hydrology Symposium*; IAHS-AISH Publication: Oxfordshire, UK, 2012; pp. 171–174.
30. Barker, J.B.; Heeren, D.M.; Neale, C.M.; Rudnick, D.R. Evaluation of variable rate irrigation using a remote-sensing-based model. *Agric. Water Manag.* **2018**, *203*, 63–74. [CrossRef]
31. Chávez, J.L.; Neale, C.; Prueger, J.H.; Kustas, W.P. Daily evapotranspiration estimates from extrapolating instantaneous airborne remote sensing ET values. *Irrig. Sci.* **2008**, *27*, 67–81. [CrossRef]
32. Ham, J.M. Useful equations, and tables in micrometeorology. *Micrometeorol. Agric. Syst.* **2005**, *47*, 533–560.
33. Atmospheric Correction Parameter Calculator. Available online: http://atmcorr.gsfc.nasa.gov/ (accessed on 25 April 2019).
34. Brunsell, N.A.; Gillies, R.R. Incorporating surface emissivity into a thermal atmospheric correction. *Photogramm. Eng. Remote Sens.* **2002**, *68*, 1263–1270.
35. Allen, R. Quality Assessment of Weather Data and Micrometeological Flux. Impacts on Evapotranspiration Calculation. *J. Agric. Meteorol.* **2008**, *64*, 191–204. [CrossRef]
36. Monteith, J.L. Solar radiation and productivity in tropical ecosystems. *J. Appl. Ecol.* **1972**, *9*, 747–766. [CrossRef]
37. Xiao, X.; Zhang, Q.; Braswell, B.; Urbanski, S.; Boles, S.; Wofsy, S.; Moore, B., III; Ojima, D. Modeling gross primary production of temperate deciduous broadleaf forest using satellite images and climate data. *Remote Sens. Environ.* **2004**, *91*, 256–270. [CrossRef]
38. Vuolo, F.; Żółtak, M.; Pipitone, C.; Zappa, L.; Wenng, H.; Immitzer, M.; Weiss, M.; Baret, F.; Atzberger, C. Data service platform for Sentinel-2 surface reflectance and value-added products: System use and examples. *Remote Sens.* **2016**, *8*, 938. [CrossRef]
39. Gorelick, N.; Hancher, M.; Dixon, M.; Ilyushchenko, S.; Thau, D.; Moore, R. Google Earth Engine: Planetary-scale geospatial analysis for everyone. *Remote Sens. Environ.* **2017**, *202*, 18–27. [CrossRef]
40. Power Data Access Viewer. Available online: https://power.larc.nasa.gov/data-access-viewer/ (accessed on 21 December 2021).
41. Kiniry, J.R.; Jones, C.A.; O'toole, J.C.; Blanchet, R.; Cabelguenne, M.; Spanel, D.A. Radiation-use efficiency in biomass accumulation prior to grain-filling for five grain-crop species. *Field Crops Res.* **1989**, *20*, 51–64. [CrossRef]
42. Goh, E.H.; Ng, J.L.; Huang, Y.F.; Yong, S.L. Performance of potential evapotranspiration models in Peninsular Malaysia. *J. Water Clim. Chang.* **2021**, *12*, 3170–3186. [CrossRef]
43. Singh, R.K.; Liu, S.; Tieszen, L.; Suyker, A.E.; Verma, S.B. Estimating seasonal evapotranspiration from temporal satellite images. *Irrig. Sci.* **2012**, *30*, 303–313. [CrossRef]
44. Neale, C.M.; Geli, H.M.; Kustas, W.P.; Alfieri, J.G.; Gowda, P.H.; Evett, S.R.; Prueger, J.H.; Hipps, L.E.; Dulaney, W.P.; Chávez, J.L.; et al. Soil water content estimation using a remote sensing-based hybrid evapotranspiration modeling approach. *Adv. Water Resour.* **2012**, *50*, 152–161. [CrossRef]
45. Geli, H.M.; Gonzalez-Piqueras, J.; Torres, E.; Campos, I.; Neale, C.M.; Calera, A. The application of a Hybrid Evapotranspiration approach in rainfed wheat. In Proceedings of the European Geosciences Union General Assembly 2013, Vienna, Austria, 7–12 April 2013; p. EGU2013-6930.
46. Bispo, R.C.; Hernandez, F.B.; Gonçalves, I.Z.; Neale, C.M.; Teixeira, A.H. Remote sensing-based evapotranspiration modeling for sugarcane in Brazil using a hybrid approach. *Agric. Water Manag.* **2022**, *271*, 107763. [CrossRef]
47. Chukalla, A.D.; Krol, M.S.; Hoekstra, A.Y. Green and blue water footprint reduction in irrigated agriculture: Effect of irrigation techniques, irrigation strategies and mulching. *Hydrol. Earth Syst. Sci.* **2015**, *19*, 4877–4891. [CrossRef]
48. Silva, B.B.; Mercante, E.; Boas, M.A.; Wrublack, S.C.; Oldoni, L.V. Satellite-based ET estimation using Landsat 8 images and SEBAL model. *Rev. Ciência Agron.* **2018**, *49*, 221–227. [CrossRef]
49. Beg, A.A.; Al-Sulttani, A.H.; Ochtyra, A.; Jarocińska, A.; Marcinkowska, A. Estimation of evapotranspiration using SEBAL algorithm and Landsat-8 data—A case study: Tatra mountains region. *J. Geol. Resour. Eng.* **2016**, *6*, 257–270.
50. Doorenbos, J.; Kassam, A.H. Yield response to water. *Irrig. Drain. Pap.* **1979**, *33*, 257.
51. Bastiaanssen, W.G.; Ali, S. A new crop yield forecasting model based on satellite measurements applied across the Indus Basin, Pakistan. *Agric. Ecosyst. Environ.* **2003**, *94*, 321–340. [CrossRef]
52. Ram, K. Levels of agricultural productivity in Haryana state 2012–2015. *Int. J. Interdiscip. Res. Arts Humanit.* **2017**, *2*, 228–232.
53. Lobell, D.B.; Hicke, J.A.; Asner, G.P.; Field, C.B.; Tucker, C.J.; Los, S.O. Satellite estimates of productivity and light use efficiency in United States agriculture, 1982–1998. *Glob. Chang. Biol.* **2002**, *8*, 722–735. [CrossRef]
54. VanDam, J.C.; Singh, R.; Bessembinder, J.J.; Leffelaar, P.A.; Bastiaanssen, W.G.; Jhorar, R.K.; Kroes, J.G.; Droogers, P. Assessing options to increase water productivity in irrigated river basins using remote sensing and modelling tools. *Water Resour. Dev.* **2006**, *22*, 115–133. [CrossRef]
55. Zwart, S.J.; Leclert, L.M. A remote sensing-based irrigation performance assessment: A case study of the Office du Niger in Mali. *Irrig. Sci.* **2010**, *28*, 371–385. [CrossRef]
56. Meena, R.P.; Sharma, R.K.; Chhokar, R.S.; Chander, S.; Tripathi, S.C.; Kumar, R.; Sharma, I. Improving water use efficiency of rice-wheat cropping system by adopting micro-irrigation systems. *Int. J. Bio-Resour. Stress Manag.* **2015**, *6*, 341–345. [CrossRef]
57. Pradhan, S.; Sehgal, V.K.; Sahoo, R.N.; Bandyopadhyay, K.K.; Singh, R. Yield, water, radiation, and nitrogen use efficiencies of wheat (*Triticum aestivum*) as influenced by nitrogen levels in a semi-arid environment. *Indian J. Agron.* **2014**, *59*, 69–77. [CrossRef]

58. Hussain, I.; Sakthivadivel, R.; Amarasinghe, U. Land, and water productivity of wheat in the Western Indo-Gangetic plains of India and Pakistan: A comparative analysis. In *Water Productivity in Agriculture: Limits and Opportunities for Improvement*; CABI Publishing: Wallingford, UK, 2003; pp. 255–271.
59. Singh, R.; Van Dam, J.C.; Feddes, R.A. Water productivity analysis of irrigated crops in Sirsa district, India. *Agric. Water Manag.* **2006**, *82*, 253–278. [CrossRef]